The Effects of Differential Diffusion in Counter-flow Premixed Flames with Dilution and Hydrogen Enrichment

Ehsan Abbasi-Atibeh[a,*], Jeffrey M. Bergthorson[a]

[a]*Department of Mechanical Engineering, McGill University, Montreal, QC H3A 0C3, Canada*

Abstract

The effects of differential diffusion on local flamelet velocities, turbulent burning rates, and structure of lean turbulent premixed flames in the thin reaction zone regime are investigated using aerodynamically stabilized flames in a counter-flow apparatus. Various fuel-oxidizer-inert mixtures with different transport properties, representative of distinct effective Lewis numbers, are studied. In order to minimize the effects of mixture reactivity in these experiments, unstretched laminar flame speed is kept constant during mixture dilution, and hydrogen enrichment of hydrocarbon flames, through changing the mixture equivalence ratio. Furthermore, bulk-flow properties and stagnation surface temperature are kept constant; hence, the study focuses on the effects of differential diffusion, which is the change in transport properties of the mixture, i.e., fuel and heat diffusivities, in the context of fuel flexibility. Highly strained laminar flame measurements are also reported as a reference of comparison. Local instantaneous statistics of various flame parameters within the imaged plane, such as flame location, flame velocity, and flame-front topology, are quantified using high-speed particle image velocimetry (PIV) and Mie scattering flame tomography at two levels of turbulence intensity. These parameters are presented as probability density functions using sufficiently large data sets to ensure statistical accuracy. The results for various flame-parameter statistics, which are measured over a wide range of Lewis numbers, show that the effects of differential diffusion are important in turbulent flames in the thin reaction zone regime. At constant turbulence intensity, differential diffusion increases the burning rates of turbulent flames in thermo-diffusively unstable mixtures through two main mechanisms: (1) increasing local flamelet displacement velocity, and (2) increasing flame-surface area. The relative contribution of these two parameters in increasing turbulent burning rates is approximately 76 % and 24 %, respectively, which is not dependent on the fuel, oxidizing-gas mixture, or turbulence intensity, and the results overlap over a wide range of Lewis numbers.

Keywords:
Differential diffusion, Fuel flexibility, Hydrogen enrichment, Lewis number, Premixed turbulent combustion, Flame surface area

*Address all correspondence to ehsan.abbasi@mail.mcgill.ca (E. Abbasi-Atibeh).

1. Introduction

The continued combustion of fossil fuels to fulfill global energy demand is being questioned because of the well-known problem of greenhouse-gas (GHG) emissions and pollutants, such as nitric oxides (NO_x), carbon monoxide (CO), and soot. Consumption of fossil fuels needs to be reduced as it introduces new carbon, in the form of carbon dioxide (CO_2), into the environment causing climate change. However, the inherent advantages of combustion-based engines in some application areas make it challenging for other power systems to compete. For instance, combustion of liquid fuels remains attractive for transportation because of the high energy density. A leading strategy is to reduce burning fossil fuels by using hydrogen (H_2) and renewable biofuels, such as biogas, syngas, and alcohols, that can be produced from conversion of various renewable energy sources, such as solar, water, wind, or geothermal, into chemical energy [1–5].

Adaptability with renewable alternative fuels that have variable compositions is referred to as *fuel flexibility*, which is an important parameter of next-generation combustor design. Fuel flexibility will, ultimately, result in higher-performance fuel-flexible combustors that lower costs of energy production, while reducing emissions and the carbon footprint of various energy technologies; hence, mitigating global climate change. However, changing fuels significantly affects combustor operability properties, such as blow out, flash back, and dynamic stability, mainly due to variations in turbulent burning rates. This manifests both as difficulties in heuristically designing fuel-flexible combustors and inaccuracy/unreliability in numerical techniques for simulating combustor behavior using computational fluid dynamic (CFD) simulations.

Changing the fuel and oxidizer mixture composition affects flame characteristics and burning rates through changing: (1) mixture reactivity, and (2) mixture diffusivity. Fuel flexibility changes chemical properties and the reactivity of the mixture, which can be represented by unstretched laminar flame speed ($S_{\mathrm{L}}^{\mathrm{o}}$) as an intrinsic property of a given fuel and oxidizer mixture. The effects of mixture reactivity on flame speed are well studied, e.g., laminar flame studies of H_2-enriched hydrocarbon flames [6–10] show that adding H_2, which is a very reactive fuel with a high laminar flame speed, to the fuel mixture enhances the flame speed, and extends the flammability limit towards the lean side enabling the engine to operate at leaner conditions. Fuel flexibility also changes the transport properties of the mixture, which are the diffusivity of the deficient reactant (fuel in lean, and oxidizer in rich, combustion) ($\mathcal{D}$) and the diffusivity of heat (α). The disparity between α and $\mathcal{D}$ at the flame front is known as *differential diffusion*, which is represented by the Lewis number ($\mathrm{Le} = \alpha/\mathcal{D}$).

Differential diffusion causes stretch sensitivity in the flame-front propagation leading to thermal-diffusive (TD) instabilities. Stretch rate (K), is defined as the normalized differential change in flame-surface area (FSA) as a function of time: $K = (1/A)\,(\mathrm{d}A/\mathrm{d}t)$ [11], which is a function of flame curvature (κ) and hydrodynamic strain ($K_{\mathrm{s-t}}$) (tangential strain rate due to a non-uniform flow field across the flame) [12]:

$$K = \kappa\, S_{\mathrm{T}} + K_{\mathrm{s-t}} \tag{1}$$

where S_T is the local characteristic flame velocity in laboratory coordinates. Stretch sensitivity of flames is an important parameter that affects the flame structure [13–19], e.g., flame-front curvature [20, 21], and burning rates in laminar and turbulent flames [16, 22–30].

Various definitions of turbulent flame velocity in the form of consumption velocity or displacement velocity are measured and reported in [19, 31–38]. One equation that describes the turbulent burning rate is [19, 39, 40]:

$$S_{T-LC} = I_o \, S_L^o \, \frac{A_T}{A_L} \tag{2}$$

where S_{T-LC} is the turbulent burning rate (also referred to as "turbulent local consumption velocity"), I_o is the local stretch factor, which depends on differential diffusion, and A_T and A_L are the turbulent and the laminar flame-surface area, respectively. Equation 2 indicates that the effects of stretch on the propagation of turbulent premixed flames in the flamelet regime originate from two main mechanisms: (1) the effects of differential diffusion on local flamelet velocities, and (2) the effects of FSA on local and global burning rates.

Previous studies [21, 31, 37, 38, 41–47] showed that the increase in FSA alone, due to turbulence folding, (i.e., classical Damköhler's hypothesis [22]) is insufficient to explain increasing burning rates with increasing flame stretch, and that differential diffusion also affects the local burning rates of laminar [31, 41, 42] and turbulent [21, 37, 38, 43–47] flames. Some studies [26, 31, 48, 49] have explained the effects of differential diffusion by the theory of leading points, where it is assumed that the burning velocity of a turbulent premixed flame is controlled by the increased velocity of the positively curved and stretched leading points, which is particularly important for thermo-diffusively unstable mixtures with $Le < 1$. While some studies show an extreme role of differential diffusion on the structure and propagation of highly turbulent flames (e.g., [50]), some researchers state that these effects are suppressed once turbulence is strong [51, 52] due to the enhanced turbulent heat and mass transport. Controversies are also seen in the literature regarding the effects of differential diffusion and turbulence intensity on premixed flame-front structure in the thin reaction zone regime. For instance, it was shown that differential diffusion has no effect on flame-front curvature and flame-surface density, and that the flame structure is only influenced by turbulence [21, 51], while other studies illustrated significant effects of differential diffusion on flame-front structure in this regime [37, 53, 54]. Furthermore, recent studies [14, 15] showed no clear dependence of flame-surface density on turbulence intensity, whereas flame-front curvature and flame-surface density were reported to increase with increasing turbulence intensity in other experimental and numerical studies [21, 53]. Hence, there is no common understanding in the combustion literature regarding the effects of differential diffusion in the thin reaction zone regime ($1 < Ka_T < 100$ and $Da_T < 1$) [55, 56], where turbulent heat and mass transport are enhanced.

In this study, the main goal is to address the controversies mentioned above, and to provide detailed understandings on the effects of differential diffusion and turbulence intensity in the thin reaction zone regime, such as the effects of differential diffusion on flame-front curvature and flame-surface area at constant turbulence intensity, as well as the effects of turbulence intensity on flame structure. To reach this goal, experiments are performed that

are focused only on the effects of differential diffusion in the thin reaction zone regime using mixtures with very distinct effective Lewis number ($\mathrm{Le_{eff}}$) in the range of $0.3 < \mathrm{Le_{eff}} < 3.1$, and the results are analyzed using a statistical approach including significantly large datasets. Furthermore, the comprehensiveness of this study allows general conclusions on the effects of differential diffusion rather than generating fuel-specific conclusions.

The experiments are performed using strained counter-flow flames, in order to study the effects of both components of flame stretch, i.e., bulk and local hydrodynamic strain rates and local curvature [37, 38, 57–67]. Most previous studies report the combined effects of mixture reactivity and diffusivity properties on the propagation and stabilization of premixed flames. In the present experiments, S_L^o is kept constant during mixture dilution, and H_2 enrichment, through changing the mixture equivalence ratio (ϕ), in order to minimize the effects of mixture reactivity. Furthermore, bulk-flow properties and the temperature boundary conditions are also kept constant; hence, the study focuses on the effects of differential diffusion.

Two-dimensional high-speed particle image velocimetry (2D-PIV) and Mie scattering flame tomography are used to quantify the effects of differential diffusion on local flamelet velocities, burning rates, and structure of turbulent premixed flames, within the imaged plane, in the thin reaction zone regime. Data-processing tools, developed through this study, are used to quantify instantaneous local flame properties based on $\mathrm{Le_{eff}}$ variations, and statistically represent these measurements in the form of probability density functions (PDF) using sufficiently large data sets.

2. Experimental method

In these experiments, lean premixed turbulent and laminar flames with distinct $\mathrm{Le_{eff}}$ are investigated at atmospheric pressure and constant S_L^o. Lean mixtures representative of distinct Lewis number ($\mathrm{Le} = \alpha/\mathcal{D} = \lambda/(\rho c_\mathrm{p}\mathcal{D})$, where λ is the thermal conductivity, c_p is the specific heat at constant pressure, and ρ is the density of the unburned reactants) are formed by changing both fuel diffusivity (which is the deficient species in the lean mixtures under study) and thermal diffusivity of the mixture. In this study, light to heavier fuels of hydrogen (H_2), methane (CH_4), and propane (C_3H_8), as well as light to heavier diluents of helium (He), nitrogen (N_2), and carbon dioxide (CO_2) are considered. In order to change the fuel diffusivity, H_2 is added into C_3H_8 in various volume ratios up to pure H_2, and in order to change the thermal diffusivity of the mixture, some of the N_2 in air, 40 % by volume, is replaced by He or CO_2. In all experiments, S_L^o is kept constant at 0.115 m/s, through changing ϕ. A CH_4+air flame at $\phi = 0.6$ and $\mathrm{Le_{eff}} \approx 1$ is selected as a reference flame with predicted $S_\mathrm{L}^\mathrm{o} = 0.115$ m/s at 300 K, and $T_\mathrm{ad} = 1669$ K. The reference flame and the corresponding S_L^o, and the amount of dilution (40 % by volume), are selected so that it is possible to stabilize a wide range of lean flames with significantly different α and fuel reactivity at constant $S_\mathrm{L}^\mathrm{o} = 0.115$ m/s, and to prevent/delay flash back. In these experiments, mixtures are prepared using specialty-gas mixtures, which contain 21 % O_2 and 79 % CO_2 (by volume), as well as 21 % O_2 and 79 % He (by volume), and the O_2 concentration in the

Table 1: Mixture properties and experimental conditions at $S_L^o = 0.115\,\mathrm{m/s}$.

	Mixtures			Mixture properties			Experimental conditions							
	Fuel [%] (Vol.)	O_2 balance diluent [%] (Vol.)	Diluent [%] (Vol.)	ϕ	T_{ad} (K)	Le_{eff}	u'^*/S_L^o	$u'^*/\overline{U}$	L/δ_L	L/η^*	δ_T/δ_L	Re_T^*	Ka_T^*	Da_T^*
High turbulence	C_3H_8	21	$60\,N_2 + 40\,He$	0.45	1513	3.08	13.7	0.33	3.6	23.1	12.4	65.7	41.4	0.3
	C_3H_8	21	N_2	0.56	1631	1.87	12.2	0.32	6.9	27.5	23.5	83.1	15.8	0.6
	C_3H_8	21	$60\,N_2 + 40\,CO_2$	0.79	1823	1.69	13.4	0.34	8.5	36.0	29.9	118.8	17.8	0.6
	$80\,C_3H_8 + 20\,H_2$	21	$60\,N_2 + 40\,CO_2$	0.77	1795	1.43	12.7	0.31	8.1	33.6	25.8	108.4	17.1	0.6
	$60\,C_3H_8 + 40\,H_2$	21	$60\,N_2 + 40\,CO_2$	0.75	1762	1.16	12.2	0.31	6.9	29.0	27.4	89.2	17.9	0.6
	$40\,C_3H_8 + 60\,H_2$	21	$60\,N_2 + 40\,CO_2$	0.71	1709	0.89	13.1	0.31	6.3	29.3	25.6	90.1	21.8	0.5
	$20\,C_3H_8 + 80\,H_2$	21	$60\,N_2 + 40\,CO_2$	0.63	1617	0.62	13.0	0.33	6.7	31.7	26.0	100.5	22.3	0.5
	$10\,C_3H_8 + 90\,H_2$	21	$60\,N_2 + 40\,CO_2$	0.57	1532	0.48	12.8	0.33	6.8	32.3	25.0	102.7	22.6	0.5
	CH_4	21	$60\,N_2 + 40\,He$	0.47	1542	1.60	14.0	0.35	3.7	23.9	12.9	68.9	42.8	0.3
	CH_4	21	N_2	0.60	1669	0.98	12.9	0.34	6.3	27.5	23.0	82.9	19.2	0.5
	CH_4	21	$60\,N_2 + 40\,CO_2$	0.88	1896	0.86	13.1	0.34	7.5	33.8	26.2	109.3	20.2	0.6
Low turbulence	C_3H_8	21	$60\,N_2 + 40\,CO_2$	0.79	1823	1.69	8.7	0.23	9.1	27.4	21.5	82.8	9.1	1.0
	$50\,C_3H_8 + 50\,H_2$	21	$60\,N_2 + 40\,CO_2$	0.73	1740	1.02	8.5	0.20	6.5	21.5	17.4	59.6	10.8	0.8
	$20\,C_3H_8 + 80\,H_2$	21	$60\,N_2 + 40\,CO_2$	0.63	1617	0.62	8.3	0.20	6.3	21.5	15.6	59.8	11.6	0.8
	H_2	21	$60\,N_2 + 40\,CO_2$	0.48	1440	0.35	8.8	0.23	5.5	22.3	17.9	62.8	16.3	0.6

* Properties are calculated upstream of the flame brush, in the preheat zone at $T \approx 576\,\mathrm{K}$.

oxidizer-inert mixture is kept constant at 21 %. The mass-averaged bulk-flow velocity at the nozzle exit is also kept constant in all experiments at 4 m/s.

Mixture properties, diffusive flame thickness ($\delta_L = \lambda/(c_p\,\rho_u S_L^o)$), as well as S_L^o values are calculated using free-flame simulations in Cantera [68]. GRI-Mech 3.0 reaction mechanism is used for CH_4 and pure H_2 computations, and AramcoMech 1.3 reaction mechanism is used for computations involving C_3H_8. The former is commonly used for CH_4 flame calculations, and the latter includes C3 chemistry required for C_3H_8 flame calculations. In H_2-enrichment experiments, Le_{eff} is defined based on the volumetric-fraction-weighted average of the Lewis numbers of the two fuels [69]: $Le_{eff} = X_{C_nH_m} Le_{C_nH_m} + X_{H_2} Le_{H_2}$, where X is the mole fraction in the fuel stream. Properties of the mixtures are presented in Table 1. To name different mixtures throughout this text, O_2 and N_2 are eliminated for brevity, as they exist in all mixtures under study. For instance, the C_3H_8+O_2+N_2+He mixture is summarized as C_3H_8+He. The pure hydrogen flame, H_2+CO_2, ($S_L^o = 0.115\,\mathrm{m/s}$ and $\phi = 0.48$) at the higher turbulence intensity case is not reported due to flash back, whereas, it is included in laminar flames, and in turbulent flames at the lower turbulence intensity.

In these experiments, Le_{eff} varies within the range of $0.3 < Le_{eff} < 3.1$, where H_2+CO_2 and C_3H_8+He flames correspond to the smallest and the largest Le_{eff}, respectively. As listed in Table 1, ϕ and the adiabatic flame temperature (T_{ad}) of the mixtures are within the range of $0.45 \leq \phi \leq 0.88$ and $1440\,\mathrm{K} \leq T_{ad} \leq 1896\,\mathrm{K}$, respectively. In all experiments, the total flow rates of the bottom nozzle, the top nozzle, at the co-flow are approximately 73.5 SLPM

(standard liter per minute), 35.2 SLPM, and 167 SLPM, respectively. Sample flow rates in H_2-enriched C_3H_8 flame with 20 % H_2 content diluted in CO_2 (80 C_3H_8+20 H_2+CO_2) are approximately 2.2 SLPM, 0.6 SLPM, 14.8 SLPM, 33.5 SLPM, and 22.3 SLPM for C_3H_8, H_2, O_2, N_2, and CO_2, respectively.

2.1. Hot-exhaust opposed-flow turbulent flame rig

The experiments are carried out using aerodynamically stabilized lifted flames in a hot-exhaust opposed-flow turbulent flame rig (HOTFR) [37, 38, 58, 61, 62, 64–67]. The burner setup is designed to stabilize premixed laminar and turbulent flames of mixtures flowing from the bottom nozzle against a stream of hot combustion products flowing from a pre-burner inside a ceramic nozzle at the top, in an axial opposed-flow configuration. A co-flow of He is used to shroud the reacting mixture and the flame from surrounding air in order to reduce the effect of the shear layer and stabilize the flame edge. A schematic of the burner setup is shown in Fig. 1. In this configuration, laminar flames are stretched mainly due to bulk strain rate (K_s) while, in turbulent flames, stretch is due to both bulk strain rate and the stretch effects of turbulent eddies through increasing flamelet curvature (κ).

The rig has a compact design with well-defined boundary conditions and excellent optical accessibility. In HOTFR, the lifted flames are not affected by conductive heat loss to the burner, and the stagnation plane of hot products allows stabilization of near-adiabatic laminar and turbulent flames. Furthermore, this configuration allows highly strained flames to be stabilized at higher bulk-flow velocities, turbulence intensities, and Karlovitz numbers in the thin reaction zone regime of the Borghi diagram [55, 56], and closer to relevant conditions of gas-turbine engines (GTE) and other combustors. These characteristics enable high-resolution laser diagnostic imaging for velocity field measurements, capturing the overall flame structure, and integral scales of highly stretched flames; hence, make the rig convenient both for diagnostics and validating computational fluid dynamic (CFD) models.

At the bottom section, two concentric inner and outer nozzles deliver the premixed fuel-oxidizer mixture, and the co-flow, respectively, through two separate concentric plena. The inner fuel-oxidizer nozzle has an exit diameter of $d_N = 20\,\text{mm}$, which is attached to the inner plenum of diameter 60 mm, with a contraction ratio of 9:1. The interior contour of the nozzle contraction is defined by polynomials that minimize the formation of Taylor-Görtler vortices [70] in the concave portion of the profile, and minimize the angle-of-attack in the convex portion [71]. This contoured design minimizes flow instabilities, and dampens the transition to turbulence, which makes the rig suitable for accurate laminar flame experiments when the turbulence-generating system is removed (e.g., [42]).

Turbulence is generated using a star-shaped high-blockage turbulence-generating plate (S-TGP) with an open area of 2.4 % [65, 72]. The S-TGP is designed to deliver the highest possible turbulence intensity while producing nearly isotropic turbulence and axisymmetric uniformity. In turbulent experiments, the S-TGP is located at vertical distances upstream of the nozzle exit of $h_1 = 142\,\text{mm}$ and $h_2 = 212\,\text{mm}$, corresponding to the higher and the lower turbulence intensity levels, respectively, since steady-state turbulence decays with distance. Therefore, two different turbulence intensities are achievable at a constant bulk-flow velocity

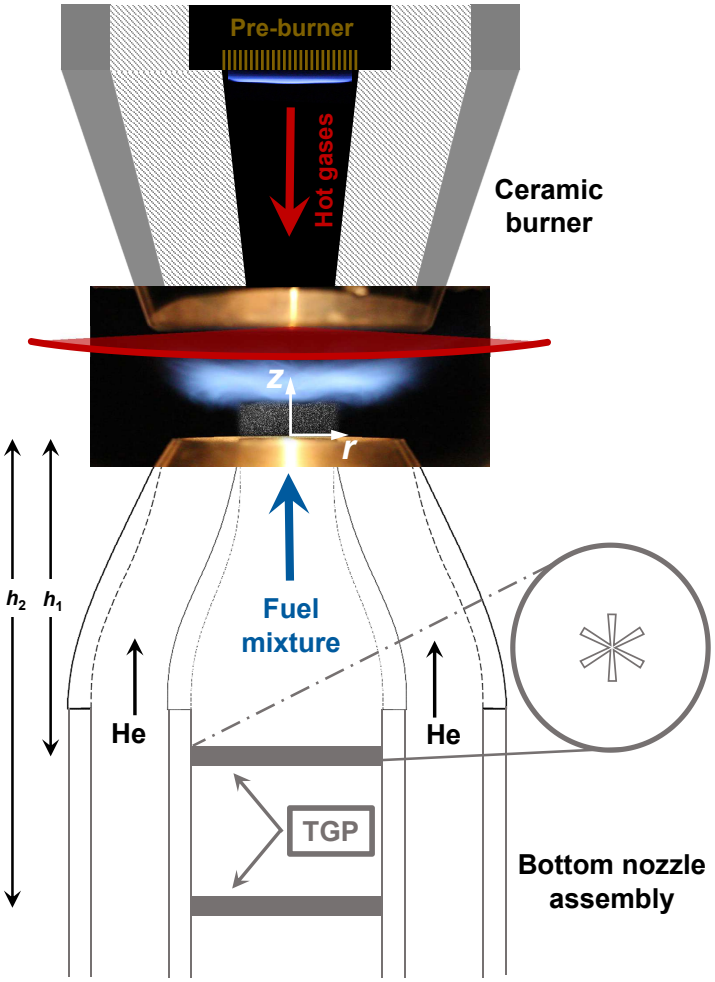

Figure 1: Schematic of HOTFR. S-TGP is located upstream of the nozzle contraction, in the inner plenum, at two different distances from the nozzle exit: $h_1 = 142\,\text{mm}$ and $h_2 = 212\,\text{mm}$.

and bulk hydrodynamic strain rate, as indicated in Table 1. In laminar flame experiments, the S-TGP is removed without changing the flow conditions or mixture compositions.

In order to minimize any bulk-flow oscillations in turbulent experiments, the S-TGP distance from the nozzle exit is set at $h_1/d_{\text{TGP}} = 2.4$ and $h_2/d_{\text{TGP}} = 3.5$, where d_{TGP} is the effective diameter of the S-TGP. This distance is chosen to be larger than that found to minimize large-scale bulk-flow oscillations, as shown in [72]. Using the energy spectra of S-TGP for various h, it was illustrated [72] that the bulk-flow oscillations (bumps in the region of low frequency energy) tend to disappear with increasing h to an optimum value of $h/d_{\text{TGP}} \gtrsim 2.3$. Furthermore, using a single-jet TGP design minimizes the pulsation of the axial jet velocity at the nozzle exit, caused by vortex-shedding from the holes of the TGP [73].

At the top section, a CH_4-air flame at $\phi = 0.7$ and $T_{\text{ad}} = 1842\,\text{K}$ is stabilized inside a

ceramic nozzle, on a flame holder, and at a vertical distance from the ceramic nozzle exit of 90 mm, as illustrated in Fig. 1. Hot exhaust gases from the pre-burner are accelerated to the test domain through the ceramic nozzle with a contraction ratio of 6.25:1. The momentum balance of the impinging flows from the top and the bottom nozzles sets the location of the stagnation plane. The separation distance between the two nozzles (h_{N}) is $1.225\,d_{\mathrm{N}}$ to minimize bulk-flow oscillations, reduce mixing with the inert co-flow or surrounding air, and maintain high strain rates.

The temperature of hot exhaust gases at the ceramic nozzle exit (T_{CB}) is measured for each experiment using R-type thermocouples with three different wire (bead) diameters at a distance of 5 mm from the nozzle exit. Temperature readings are corrected for heat losses by extrapolating the measured temperatures to a zero bead diameter [74, 75]. The velocity and temperature of the hot exhaust gases at the ceramic nozzle exit are kept constant at $U_{\mathrm{CB}} \approx 12\,\mathrm{m/s}$ and $T_{\mathrm{CB}} = 1786\,\mathrm{K}$, respectively, in all laminar and turbulent flame experiments. Radial temperature profiles are nearly constant, and the repeatability in measuring T_{CB} is $\approx 1\,\%$ of the reading. The effects of deviations from adiabatic conditions at the stagnation surface ($\mid T_{\mathrm{CB}} - T_{\mathrm{ad}} \mid$) on flame speed are discussed in the Supplementary Material.

Fuels, oxidizing-gas mixtures, and inerts are delivered using mass flow controllers (MFC) at room temperature, which are calibrated using a Bios DryCal ML-800-44 dry-piston calibrator before each set of runs. Through this calibration process, the absolute uncertainty in mixture composition is reduced to $\approx 0.9\,\%$.

2.2. Diagnostic method and processing techniques

2.2.1. Particle image velocimetry

Velocity fields are measured in laminar and turbulent experiments using two-dimensional high-speed particle image velocimetry (2D-PIV) within the imaged plane. In PIV, oil droplets ($\approx 1\,\mu$m) are atomized and seeded into the flow. At the test section, these droplets are illuminated using a thin sheet ($\approx 1\,$mm) of visible frequency-doubled Nd:YLF laser at 527 nm wavelength pulsing at a repetition rate of 10 kHz. The Mie scattered light is captured using a high-speed camera at an imaging speed of 10 kfps, and a resolution of 768 × 976 pixels. 8 000 and 1 000 PIV image pairs are post-processed using DaVis 8.2 in each turbulent and laminar experiment, respectively, to calculate the two-component velocity vector field within the plane of the laser sheet. The large number of images is to ensure that the results are statistically converged. Sample PIV velocity vectors of the turbulent and laminar C_3H_8+air flames are illustrated in Fig. 2.

In PIV post-processing, a larger interrogation window of size 96 × 96 pixel is refined using a grid-refinement cross-correlation technique to a 16 × 16 pixel grid in five passes with a window overlap of 75 %. The pixel-to-mm ratio is 46.6, and independent velocity data is measured at a grid-spacing equal to the smallest interrogation window size (16 pixels $\approx 343.5\,\mu$m), which is considered as the spatial resolution of PIV in measuring the velocity vectors. In order to increase the signal-to-noise ratio in calculating instantaneous axial (U) and radial (V) velocities at time t_i, three successive PIV images at t_{i-1}, t_i, and t_{i+1} are considered, and a second-order central differencing method is used to estimate particle displacement vectors at time t_i. It should be noted that local beam steering, caused by

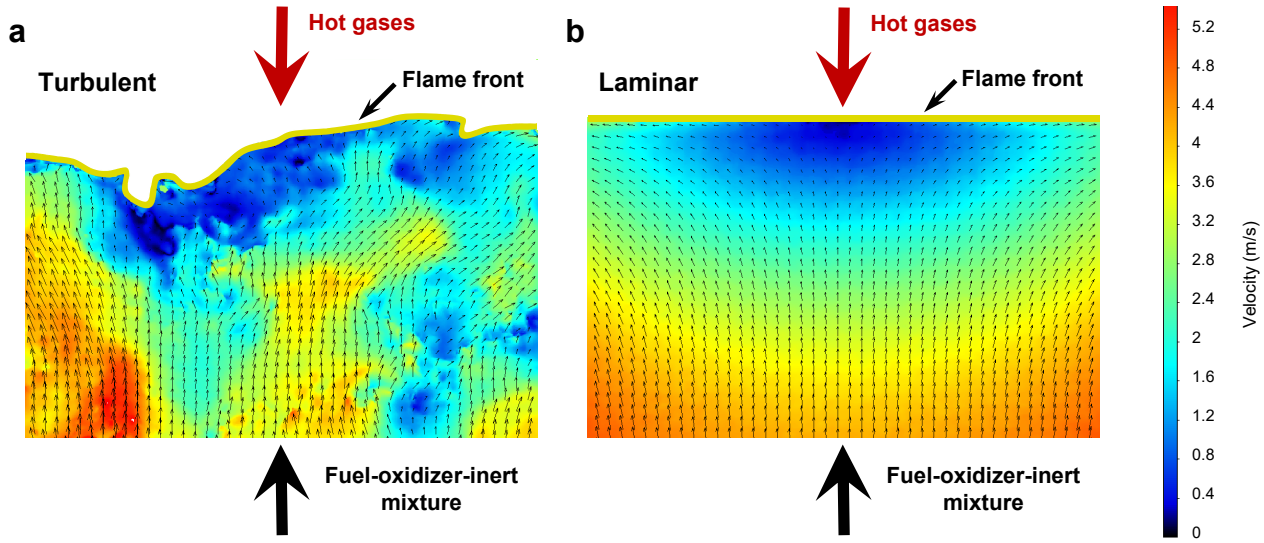

Figure 2: Sample PIV velocity vectors and flame fronts: (a) turbulent C_3H_8+air flame, and (b) laminar C_3H_8+air flame. The density of the velocity vectors is reduced by 4 times for better visibility.

gradients in refractive index due to temperature and species gradients through the flame, can negatively affect the laser intensity profile in counter-flow flame experiments [76], which could negatively affect the spatial resolution and accuracy of PIV experiments. Beam steering is shown to be exacerbated when heavy vaporized fuels are used, due to their high index of refraction, and in regions of high temperature gradients [76]. These beam-steering effects are not expected to significantly affect the present PIV measurements due to the low refractive indices of the light fuels used in this work, the lean fuel concentrations, and the moderate temperature in the preheat zone at which the velocity fields are recorded at ($T \approx 576\,\mathrm{K}$). In addition, it should be noted that PIV measurements are not extremely sensitive to variations in the laser sheet intensity profile, as compared to species or soot concentration measurements.

Uncertainties associated with PIV are calculated based on the velocity lag of tracer particles in regions of high velocity gradients due to particle inertia (relaxation time or Stokes time), as well as uncertainties originating from the processing algorithm of the PIV software. These calculations result in an uncertainty of approximately 1.5 % in the unburned gas velocity in turbulent flame experiments. Details of the uncertainty analysis in the flow velocity measurement are discussed in [38].

Turbulent flow statistics of the average flow velocity (axial, $\overline{U}$, and radial, $\overline{V}$), and the fluctuating components of the velocity (axial, u, and radial, v) are calculated from PIV data at each grid through Reynolds decomposition [77, 78]: $U(r,z,t) = \overline{U}(r,z) + u(r,z,t)$, where U is the instantaneous flow velocity at radial (r) and axial (z) location at time t. Statistics of u and v are calculated as the root-mean-square (rms) of velocity fluctuations (axial, u', and radial, v'). These results are listed in Table 1 for various mixtures, where $\overline{U}$ and u' are averaged over the test domain at 0.7 mm above the nozzle exit, and upstream of the flame brush in the preheat zone at $T \approx 576\,\mathrm{K}$ (i.e., the flash point of oil used for seeding),

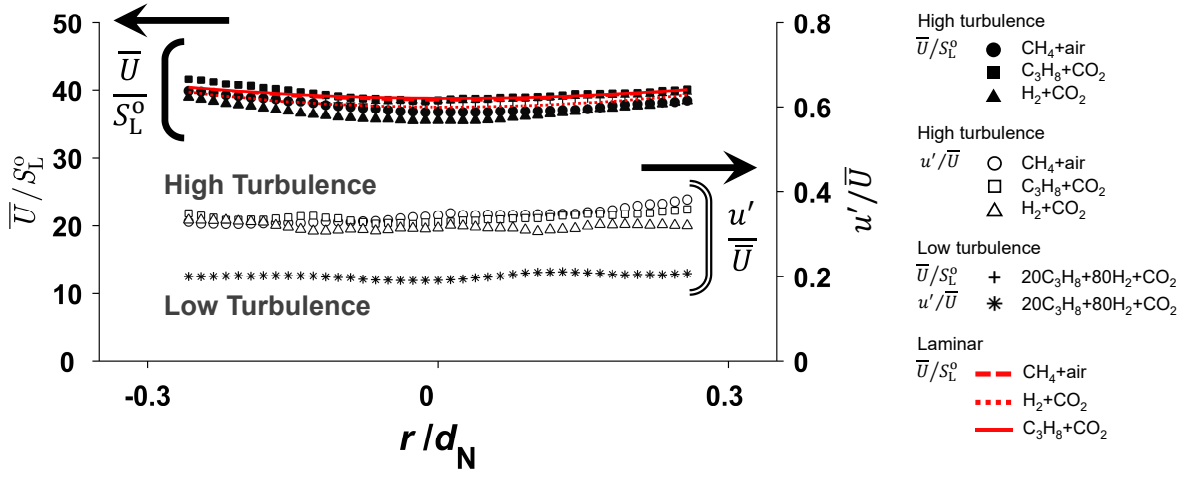

Figure 3: $\overline{U}$ and u' at the nozzle exit and upstream of the flame brush, respectively, in laminar and turbulent flames at two levels of turbulence intensity with distinct $\mathrm{Le_{eff}}$. Note that some $\overline{U}$ profiles overlap showing the uniformity of the mean flow.

respectively. Axial turbulence intensity $(u'/\overline{U})$ ranges between $31\% \leq \left(u'/\overline{U}\right) \leq 35\%$ for the higher, and $20\% \leq \left(u'/\overline{U}\right) \leq 23\%$ for the lower, turbulence levels.

The performance of the S-TGP in generating turbulence is illustrated in Fig. 3, which shows that $\overline{U}$ is almost constant in the test section in both laminar and turbulent flows, and $u'/\overline{U}$ profiles are flat in the test domain. HOTFR was previously shown [37] to produce turbulence statistics at the nozzle exit that are nearly isotropic ($u' \approx v'$). However, in a highly strained impinging-jet geometry, as the flow approaches the stagnation plane, eddies in the turbulent flow are significantly compressed and stretched. Even if the flow is isotropic at the nozzle exit, it is no longer isotropic in the flame vicinity. Similar phenomena are present in most burner technologies. The uniformity of the turbulent flow at the inlet boundary is important for future CFD modeling of these experiments.

In turbulent experiments, the integral length scale (L) is estimated by integrating the transverse autocorrelation function of u in the radial direction over the test domain, at $\approx 0.7\,\mathrm{mm}$ above the nozzle exit, from $r/d_\mathrm{N} = -0.25$ up to the first zero-crossing, as discussed in [77, 79]: $L = \int R_\mathrm{uu}(r,t)\ \mathrm{d}r$. The estimated values of L vary between $2.46\,\mathrm{mm} \leq L \leq 3.1\,\mathrm{mm}$, with the average value $\overline{L} = 2.87\,\mathrm{mm}$, which is on the order of the characteristic length of the S-TGP ($\approx 2\,\mathrm{mm}$). The scaled values of L are listed in Table 1 for various experimental conditions. An estimation of the ratio of largest to smallest hydrodynamic length scales in a turbulent flow can be derived as [77]: $L/\eta \approx \mathrm{Re_T}^{3/4}$, where η is the Kolmogorov length scale, and $\mathrm{Re_T}$ is the turbulent Reynolds number: $\mathrm{Re_T} = u'\,L/\nu$ (ν is the kinematic viscosity). $\mathrm{Re_T}$ is calculated upstream of the flame brush, in the preheat zone at $T \approx 576\,\mathrm{K}$, yielding $\mathrm{Re_T}$ values in the range of $59 \leq \mathrm{Re_T} \leq 119$, as listed in Table 1. The cold flow equivalent of $\mathrm{Re_T}$ is around 383 in the C_3H_8-CO_2 experiment. Studying

turbulence-chemistry interactions in this range of $\mathrm{Re_T}$ is of specific interest in the validation of flamelet models, in the region where mixing and chemical time scales are comparable.

Turbulent Damköhler number ($\mathrm{Da_T}$) and turbulent Karlovitz number ($\mathrm{Ka_T}$) are key quantities describing turbulence-chemistry interactions. $\mathrm{Da_T}$ relates the timescale of the turbulent transport phenomena to the chemical reaction timescale: $\mathrm{Da_T} = \tau_\mathrm{F}/\tau_\mathrm{c}$, where $\tau_\mathrm{F} = L/u'$ and $\tau_\mathrm{c} = \delta_\mathrm{L}/S_\mathrm{L}^\mathrm{o}$. $\mathrm{Ka_T}$ is defined as the ratio of τ_c and the Kolmogorov time scale (τ_η): $\mathrm{Ka_T} = \tau_\mathrm{c}/\tau_\eta$, and is calculated as: $\mathrm{Ka_T} = (L/\delta_\mathrm{L})^{-2}\ \mathrm{Re_T}^{1.5}$. $\mathrm{Ka_T}$ indicates the tendency of the eddies to penetrate into the preheat zone of the flame and, along with velocity and length scale ratios, defines different regimes of turbulent combustion in the Borghi diagram [55, 56]. In investigating flame-vortex interactions, the high-temperature zone near the flame front affects $\mathrm{Re_T}$, $\mathrm{Ka_T}$, and $\mathrm{Da_T}$ calculations; therefore, these temperature-sensitive parameters are calculated immediately upstream of the flame brush. In these experiments, $\mathrm{Da_T}$ and $\mathrm{Ka_T}$ range between $0.3 \leq \mathrm{Da_T} \leq 1$ and $9.1 \leq \mathrm{Ka_T} \leq 42.8$, respectively, showing that these flames are located in the thin reaction zone regime.

2.2.2. Processing techniques

Particle image velocimetry and Mie scattering flame tomography allow simultaneous flame-location and velocity-field measurements [37, 38, 40, 80, 81], which enables time-resolved study of the turbulence-chemistry interactions. Atomized oil droplets are seeded into the flow as tracer particles, and then evaporate at the flame front and terminate the Mie scattering of light. Flame-surface tracking methods, developed in this study, are used to localize and track the flame-front motion. The instantaneous flame location within the imaged plane (Z_f) is determined in each frame by tracking the regions of maximum intensity gradients at the flame front using the Pavlidis edge-finding algorithm [37, 38, 82]. A sample PIV image and the flame front are illustrated in Figs. 4a and 4b. Within the plane of the laser sheet, the origin of the 2D coordinate system is located at the center of the bottom nozzle, where r is the radial direction and the z-axis is normal to the exit plane of the bottom nozzle, and the radial boundaries of the test domain are between $-0.25 \leq (r/d_\mathrm{N}) \leq 0.25$. The main uncertainty sources in finding instantaneous flame location are average tracer particle distance in the test domain, oil droplet lifetime at the flame front, uncertainties imposed by filtering processes during the post-processing procedure, and over-saturated pixels from larger oil droplets in PIV images, resulting in a total uncertainty of less than $0.5\,\delta_\mathrm{L}$. The details of the uncertainty analysis in flame-front tracking are discussed in [38].

The instantaneous flame-location measurements are used to estimate the increase in FSA of turbulent flames compared to that of a laminar flame: $\Sigma = A_\mathrm{T}/A_\mathrm{L}$. Since these measurements are based on 2D-PIV within the plane of the laser sheet, an estimate of Σ is possible by a direct measurement of the length of the 2D slice of the FSA (e.g., [83]). In this estimation, both flame surfaces, i.e., A_T and A_L, are calculated by multiplying the flame length in turbulent flames, and that of an idealized laminar flame with a length of $\approx 10\,\mathrm{mm}$, respectively, by the thickness of the laser sheet. However, this estimated value under-estimates the Σ, since the variations of FSA due to turbulence folding in the depth of the image is not considered. The direct numerical simulation (DNS) study of Bell *et al.* [84] illustrates that the flame surface density estimated using 2D flame surfaces under-estimates

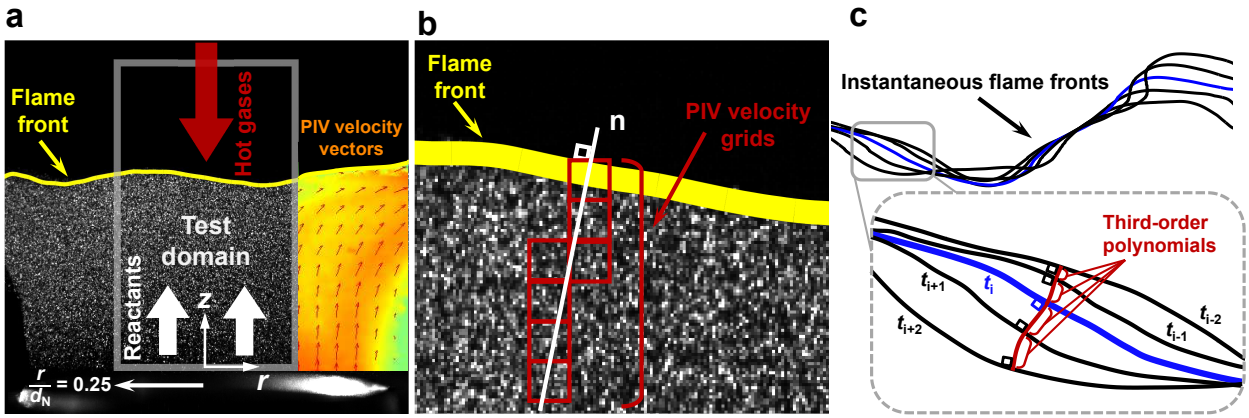

Figure 4: Processing techniques: (a) a sample PIV image indicating the test domain, an example flame front, and PIV velocity vectors (the density of the velocity vectors is reduced by 8 times for better visibility.), (b) a portion of a sample PIV image near the flame front illustrating the schematic of S_u measurement (PIV velocity vectors are available at the grid corners), and (c) 5 successive flame fronts and a schematic showing S_F calculation.

the values calculated based on 3-dimensionally resolved flame contours by 25−33 %. In this study, relative values of Σ are used to assess how differential diffusion affects flame topology and burning rates, and the 2D projection of FSA is sufficient for these purposes. Flame-front tracking methods are also used to extract 2D flame topology within the imaged plane, such as local instantaneous flame-front curvature in flame-contour coordinates and normal directions to the flame contour. Flame-front curvature is calculated as [63, 85, 86]:

$$\kappa = \frac{r'z'' - z'r''}{(r'^2 + z'^2)^{3/2}} \tag{3}$$

where first and second derivatives are calculated in flame-contour coordinates. In this study, κ is positive when a curved flamelet is convex towards the reactants.

In counter-flow flames, streamlines diverge as the flow approaches the stagnation surface, and the flames are stretched due to tangential hydrodynamic strain rate (K_{s-t}). The K_{s-t} is defined as the differential change in the unburned flow velocity as a function of distance at each location along the tangent line to the flame front, which is calculated at increments of 4 pixels in flame-contour coordinates. At each location on the flame-contour, two velocity vectors centered at this location are considered, that are at least 16 pixels apart to ensure the statistical independence of the velocity vectors. A second-order central differencing method is used to estimate K_{s-t} (compression or stretch), using projected velocities onto the tangent line and the distance between the two velocity vectors.

In Eq. 2, I_o is the ratio of the local stretched flamelet velocity to S_L^o [19, 40]. In this study, I_o is estimated as the normalized local flamelet displacement velocity in the laboratory coordinate system (S_{T-LD}): $I_o \approx S_{T-LD}/S_L^o$, which is a function of differential diffusion. In this study, S_{T-LD} is referred to as S_T for brevity. In these experiments, the flame surface is measured at the constant droplet evaporation temperature ($T \approx 576\,\mathrm{K}$), not a constant

temperature progress variable (c), due to variations in T_{ad} of the mixtures. Therefore, the exact value of I_o reported in this study might not be necessarily meaningful, but the relative trends are still important, and this dataset can be used for validation of models, as long as the "validation surface" is set to be equal to the appropriate c value for each experiment. The S_T is the propagation velocity of the local flamelet in the flow coordinate system (S_F) relative to the convective velocity of the flow (S_u) in the direction normal to the flame surface (n) [19, 37, 38, 87–89]: $S_T = (S_F + S_u) \cdot n$. In order to calculate S_T, S_u and S_F need to be determined. In this study, single-plane PIV imaging within the plane of the laser sheet measures the 2D projection of S_T within the imaged plane.

In counter-flow flames, a laminar flame stabilizes at some location where the local flow velocity matches the stretched flame speed. As the laminar jet approaches the stagnation plane, the velocity reduces and its profile shows a minimum, after which the flow accelerates through the preheat zone as the density drops due to dilatation [42]. The location of this velocity minimum is considered to be the location of flame stabilization, and this minimum value of the velocity profile ahead of the flame is taken as the reference flame speed (S_{u-ref}), which is typically used in laminar flame studies as the characteristic flame speed at the given stretch rate. In this paper, stretched laminar flame experiments are used to find the flame location and laminar stretched flame speed for comparison to the turbulent values.

In turbulent flames, the two-component velocity field upstream of the flame is used to find the convective velocity of the flow (S_u). The values of S_u are calculated using the velocity grid network in the vicinity of the normal line to the flame surface within 1.25 mm upstream of the flame front at each location along the flame contour, as illustrated in Fig. 4b. These velocity profiles may not show a local velocity minimum upstream of the flame front due to the unsteady turbulent flow and the filtering effects of flame motion; therefore, S_u is found by taking the average of the two closest velocity values to the flame surface. The S_u (or S_{u-ref}) is positive when the unburned gas velocity is towards the flame.

In order to determine local instantaneous flamelet velocity in the flow coordinate system within the imaged plane (S_F), image-processing techniques, similar to the methods proposed in [90, 91], are used. A high-order finite differencing method is used in the reconstruction of the flamelet's path between consecutive flame fronts to improve signal-to-noise ratio in S_F calculations of highly turbulent flames. To calculate S_F at time t_i, 5 successive flame fronts, 2 upstream at t_{i-2} and t_{i-1}, and 2 downstream at t_{i+1} and t_{i+2} are considered. The flamelet's path between 5 consecutive flame fronts within the imaged plane is estimated using 4 continuous third-order polynomials to reconstruct the flame motion using a continuous streamline, which is perpendicular to all 5 flame fronts, and for which the total length is a minimum. For each location along the flame contour at t_i, at increments of 4 pixels in the flame-contour coordinates, the length of a third-order polynomial is minimized between this location and the neighboring front, which is constrained by the normal direction to both fronts. The same procedure is used to determine all four third-order polynomials, which estimates the flamelet's pathway from t_{i-2} to t_{i+2}. A fourth-order finite difference method is used to estimate the displacement at each location at t_i, which is used in calculation of S_F. This method is illustrated schematically in Fig. 4c. The S_F is considered positive when the flame moves towards the unburned gas. S_F and S_u are used in the calculation of S_T.

3. Results and discussion

Experiments in this study investigate stretch sensitivity and the effects of differential diffusion on the propagation, stabilization, and structure of lean premixed flames. Various fuel-oxidizer-inert mixtures are selected at constant $S_{\mathrm{L}}^{\mathrm{o}}$, but distinct $\mathrm{Le}_{\mathrm{eff}}$, to highlight the effects of differential diffusion. Laminar flame measurements are reported for diluted C_3H_8 flames with CO_2 and He, as well as H_2-enriched C_3H_8 flames.

3.1. Flame-front location

The Z_{f} of various mixtures at a wide range of $\mathrm{Le}_{\mathrm{eff}}$ ($0.3 < \mathrm{Le}_{\mathrm{eff}} < 3.1$) are illustrated in Fig. 5 for laminar flames, as well as for turbulent flames at two different turbulence intensities. In the counter-flow geometry, the momentum balance of the impinging-jets defines the location of the stagnation plane, and flames stabilize close to the stagnation plane because of high bulk-flow velocities. The composition, temperature of hot exhaust gases (T_{CB}), and the top nozzle exit velocity (U_{CB}) are constant in these experiments, which results in a constant momentum of the hot jet in all experiments. Changing the mixture composition of the cold jet, however, changes its momentum, mainly due to variations in mixture density. Therefore, as various mixtures are produced at constant $S_{\mathrm{L}}^{\mathrm{o}}$ but distinct $\mathrm{Le}_{\mathrm{eff}}$, variations in flame location are due to the effects of both movement of the mean stagnation surface location, as well as variations in the burning rate of flames due to the effects of differential diffusion.

In order to highlight the effects of differential diffusion on burning rates, the PDFs of flame location, and the correlations of the most-probable flame location against $\mathrm{Le}_{\mathrm{eff}}$, are plotted in the stagnation-plane (SP) coordinate system, where $\langle Z_{\mathrm{SP}} \rangle - Z_{\mathrm{f}} = 0$ indicates the flame surface located at the average location of the stagnation plane and $\langle Z_{\mathrm{SP}} \rangle - Z_{\mathrm{f}}$ increases towards the bottom nozzle, as illustrated in Fig. 5. For each mixture, the stagnation-plane location is measured by Mie scattering flame tomography of the impinging jets of the hot exhaust gases and the non-reacting flow with preserved flow properties of the oxidizer-inert portion of the unburned laminar and turbulent flows. The fuel is removed from the mixtures to prevent autoignition at the stagnation surface. The presence or lack of a flame does not change the momentum of the jet and therefore, should minimally affect the location of the stagnation surface. The flame location is normalized by the separation distance between the two nozzles (h_{N}), and the standard deviation of $\langle Z_{\mathrm{SP}} \rangle$ is less than $0.029\, h_{\mathrm{N}}$ over the full set of mixtures.

PDFs of flame location at various $\mathrm{Le}_{\mathrm{eff}}$ at the higher, and the lower, turbulence intensity levels are shown in Figs. 5a and 5c, respectively. These PDFs determine the most-probable flame location ($\langle \langle Z_{\mathrm{SP}} \rangle - Z_{\mathrm{f}} \rangle$), and the flame-brush thickness (δ_{T}). Furthermore, skewness of these PDFs indicates a propensity for the instantaneous flame location to be upstream or downstream of the average location.

Variations of $\langle \langle Z_{\mathrm{SP}} \rangle - Z_{\mathrm{f}} \rangle$ for laminar flames and turbulent flames at the higher turbulence intensity are shown in Fig. 5b. As shown in Figs. 5a and 5b, PDFs of flame location overlap for $0.9 < \mathrm{Le}_{\mathrm{eff}} < 3.1$, and are skewed towards the stagnation surface, as they are pushed to the hot exhaust gases by steep average velocity gradients; hence, the most-probable flame

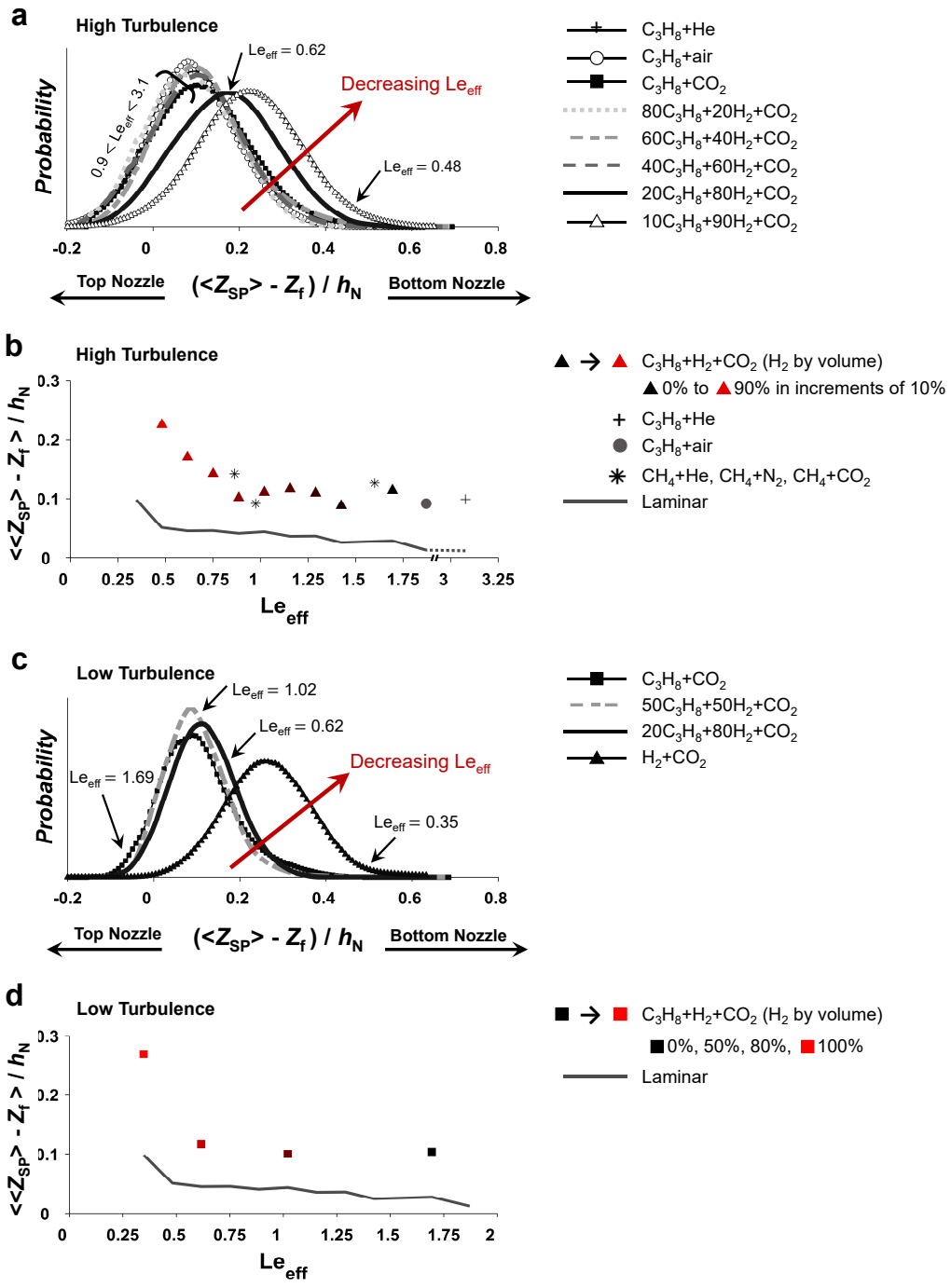

Figure 5: (a) PDFs of flame location at various $\mathrm{Le_{eff}}$, and (b) correlations of $\langle\langle Z_{\mathrm{SP}}\rangle - Z_{\mathrm{f}}\rangle$ with respect to $\mathrm{Le_{eff}}$ under the high-turbulence level. (c) and (d) PDFs of flame location and its correlations under the low-turbulence level. The x-axis is broken to show the C_3H_8-He flame at $\mathrm{Le_{eff}} = 3.08$. Laminar flame measurements are reported for diluted C_3H_8 flames with CO_2 and He, as well as H_2-enriched C_3H_8 flames. For details of the mixtures see Table 1.

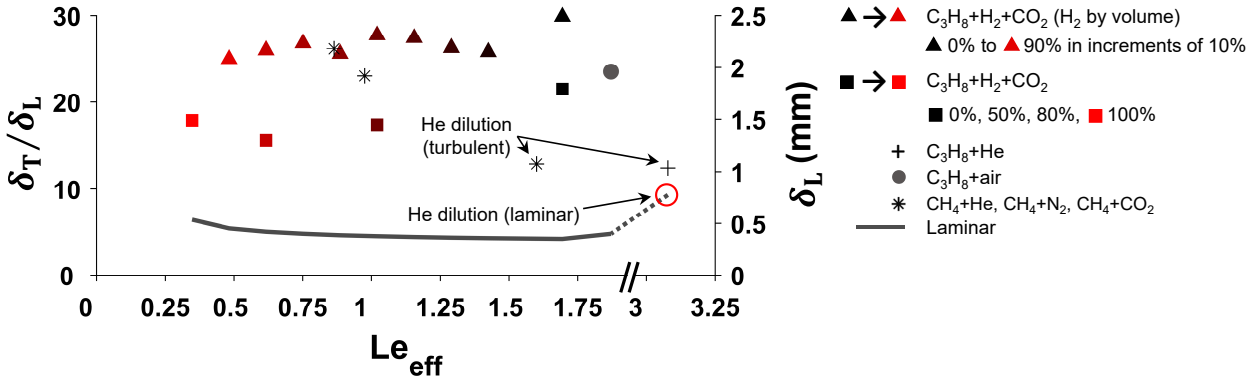

Figure 6: δ_T of turbulent and δ_L of laminar flames. Laminar flame measurements are reported for diluted C_3H_8 flames with CO_2 and He, as well as H_2-enriched C_3H_8 flames. The x-axis is broken to show the C_3H_8-He flame at $Le_{eff} = 3.08$.

location is almost constant in mixtures with $Le_{eff} > 1$. As Le_{eff} falls below unity, PDFs of flame location significantly move upstream toward the bottom nozzle with decreasing Le_{eff}, and are less skewed. This relocation is also illustrated by a significant increase in $\langle\langle Z_{SP}\rangle - Z_f\rangle$ for mixtures with $Le_{eff} \ll 1$ shown in Fig. 5b. In laminar flames at constant S_L^o, $\langle\langle Z_{SP}\rangle - Z_f\rangle$ increases linearly with a shallow slope up to $Le_{eff} \approx 0.5$, and rises significantly for the pure H_2 flame ($Le_{eff} \approx 0.35$), due to differential diffusion enhancing the stretched flame speed. In thermo-diffusively unstable turbulent flames with $Le_{eff} \ll 1$, the global burning velocity considerably increases with decreasing Le_{eff}; hence, the flames are stabilized closer to the bottom nozzle exit in the steep average bulk-flow velocity gradients. The pure H_2 flame could not be stabilized at the higher turbulence intensity due to flash back, which also shows that the turbulent burning rate is enhanced compared to the other mixtures.

Variations of $\langle\langle Z_{SP}\rangle - Z_f\rangle$ at the lower turbulence intensity are summarized in Fig. 5d for mixtures with $0.35 \leq Le_{eff} \leq 1.69$. As illustrated in Figs. 5c and 5d, PDFs of flame location at $Le_{eff} \gtrsim 1$ overlap, and the most-probable flame location is almost constant. With decreasing Le_{eff}, at $Le_{eff} \approx 0.6$, the PDF starts to move further towards the fresh reactants, and the pure H_2-CO_2 flame ($Le_{eff} = 0.35$) stabilizes at the closest distance to the bottom nozzle due to a significant increase in turbulent burning rates.

Turbulent flame-brush thickness is calculated using PDFs of flame location: $\delta_T = 4 \times \sigma$, where σ is the standard deviation of the PDFs. In Fig. 6, the scaled values of δ_T are plotted, along with the laminar flame thickness (δ_L) for reference. In general, the normalized δ_T is larger in flames at the higher turbulence intensity compared to the same mixtures at the lower turbulence intensity. At each turbulence intensity, while the dimensional values of δ_T show an increase with decreasing Le_{eff}, the scaled values appear flat because the δ_L also increases for reduced Le_{eff}. In mixtures with He dilution, δ_L is considerably larger due to the increased thermal diffusivity of the mixture ($\delta_L \propto \alpha/S_L^o$).

3.2. Local flamelet displacement velocity

PDFs of S_T for flames at two levels of turbulence intensity are illustrated in Figs. 7a−7c. These PDFs show the most-probable local turbulent flame velocity ($\langle S_T \rangle$), and the distribution of PDFs compared to S_L^o. In Fig. 7a, PDFs of S_T for C_3H_8 and H_2-enriched C_3H_8 flames at the higher turbulence intensity illustrate that the peak moves towards higher local velocities with decreasing Le_{eff} in mixtures with $Le_{eff} < 1$, and S_T significantly passes S_L^o, due to the effects of differential diffusion. However, the PDFs of mixtures with $Le_{eff} > 1$ overlap, and $\langle S_T \rangle$ is almost constant in these mixtures. PDFs of S_T for CH_4 flames at the higher turbulence intensity are illustrated in Fig. 7b, where Le_{eff} is varied through dilution with different inerts. In these flames, the peaks of the PDFs only slightly move towards higher velocities, as Le_{eff} decreases from 1.6 to 0.86. These PDFs show values in the range of $-2 \lesssim (S_T/S_L^o) \lesssim 12$, consistent with 3D turbulent displacement velocity measurements reported in [88]. At the lower turbulence intensity shown in Fig. 7c, PDFs of S_T are narrower compared to the higher turbulence case in mixtures with $Le_{eff} > 1$. With increasing H_2 enrichment in C_3H_8-CO_2 from 0 % ($Le_{eff} = 1.69$) to 100 % ($Le_{eff} = 0.35$), PDFs of S_T significantly widen and the peaks move towards higher velocities. Evidently, negative S_T values are less likely, and account for only ≈ 14 % of all S_T measurements. A DNS study of 2D stoichiometric CH_4-air flames [92] show negative S_T values in highly curved concave regions towards the reactants.

In order to quantify these effects, $\langle S_T \rangle$ of turbulent flames, as well as S_{u-ref} of laminar flames, are plotted against Le_{eff} in Fig. 7d, where $\langle S_T \rangle / S_L^o \approx \langle I_o \rangle$ (Eq. 2). S_{u-ref}/S_L^o values are larger than 1 because of stretch and hydrodynamic effects on the laminar counter-flow flames [42]. In general, $\langle S_T \rangle$ is larger than S_{u-ref}, as local curvature generated by eddies in turbulent flames enhances the local flamelet velocities. Furthermore, $\langle S_T \rangle$ is larger at the higher turbulence intensity compared to the lower intensity, due to an increase in local curvature effects with increasing turbulence intensity.

As illustrated in Fig. 7d, S_{u-ref}/S_L^o variations with decreasing Le_{eff} correlate well with the laminar flame location variations shown in Figs. 5b and 5d, with a sharp increase at $Le_{eff} \ll 1$. At the higher turbulence intensity, the normalized $\langle S_T \rangle$ is almost constant at ≈ 4 in flames with $Le_{eff} > 1$, whereas in flames with $Le_{eff} < 1$, it increases with decreasing Le_{eff} up to 5.6 for C_3H_8-CO_2 with 90 % H_2 enrichment. The S_T results are consistent with the study of Daniele *et al.* [93], who reported the local flamelet velocities for fuels ranging from CH_4 to syngas blends. In thermo-diffusively stable mixtures ($Le_{eff} > 1$), thermal diffusion from the positively stretched portion of the flame front is larger than fuel diffusion into the stretched area; hence, the rate of thermal energy loss is greater than chemical energy gain provided by molecular diffusion into the reaction zone, which decreases the temperature, and results in decreasing the flame velocity. In thermo-diffusively unstable mixtures ($Le_{eff} < 1$), at a positively stretched portion of the flame front, molecular diffusion into the stretched area is larger than thermal energy loss through heat conduction and thermal diffusion, which increases the local ϕ and temperature; hence, the velocity of the leading points increases [50]. At the lower turbulence intensity, $\langle S_T \rangle / S_L^o$ peaks at the pure H_2 flame ($Le_{eff} = 0.35$). In general, as illustrated in Fig. 7d, the effect of Lewis number on the local flame velocity of stretched flames is not linear, with sharp increases in the local flame velocity of mixtures

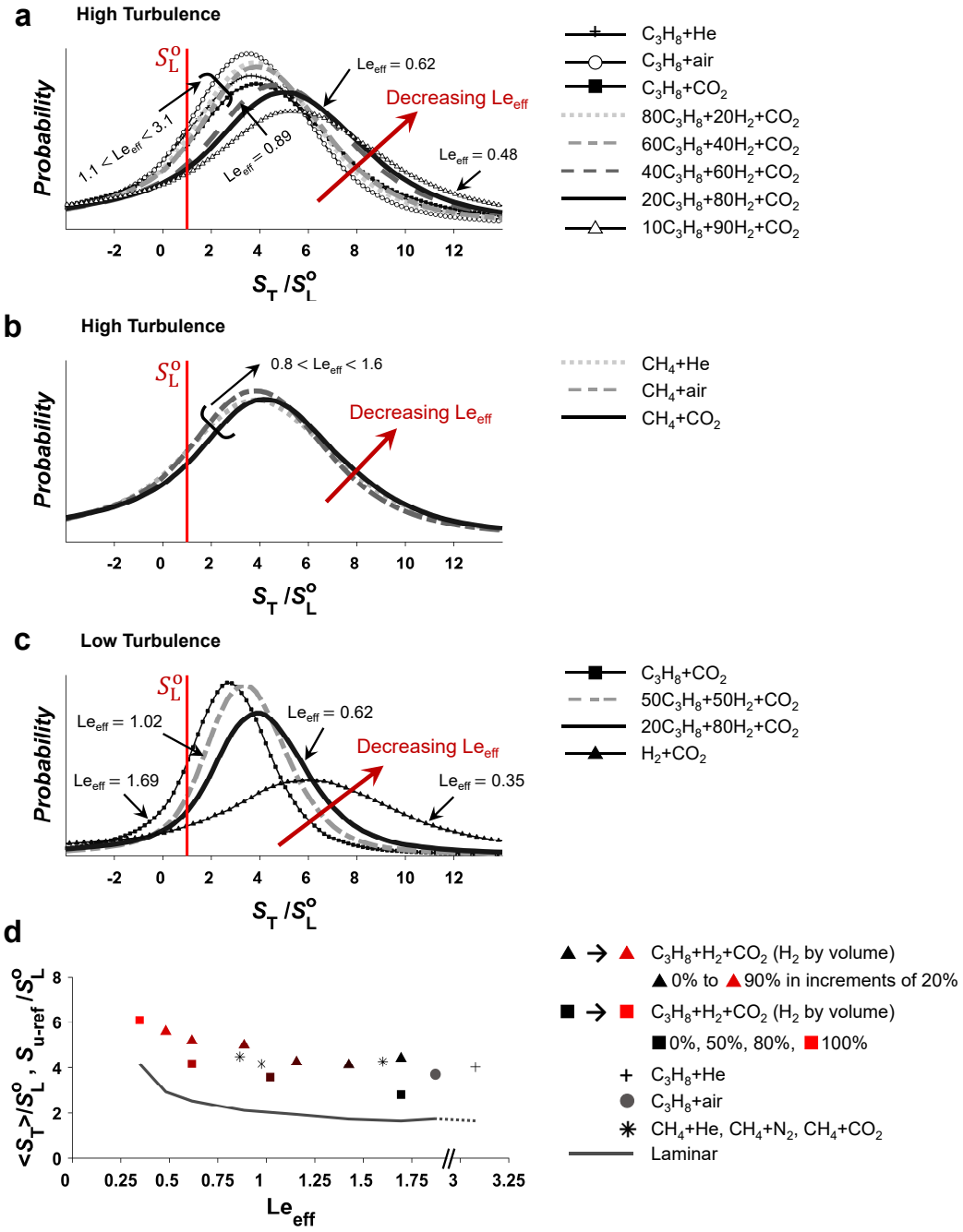

Figure 7: PDFs of S_T for flames at various Le_{eff}: (a) C_3H_8 and H_2-enriched C_3H_8 flames in various oxidizing-gas mixtures under the high-turbulence level, (b) CH_4 flames in various oxidizing-gas mixtures under the high-turbulence level, and (c) C_3H_8 and H_2-enriched C_3H_8 flames in CO_2 under the low-turbulence level. (d) Correlations of $\langle S_T \rangle$ and S_{u-ref} with respect to Le_{eff}. Laminar flame measurements are reported for diluted C_3H_8 flames with CO_2 and He, as well as H_2-enriched C_3H_8 flames. The x-axis is broken to show the C_3H_8-He flame at $Le_{eff} = 3.08$.

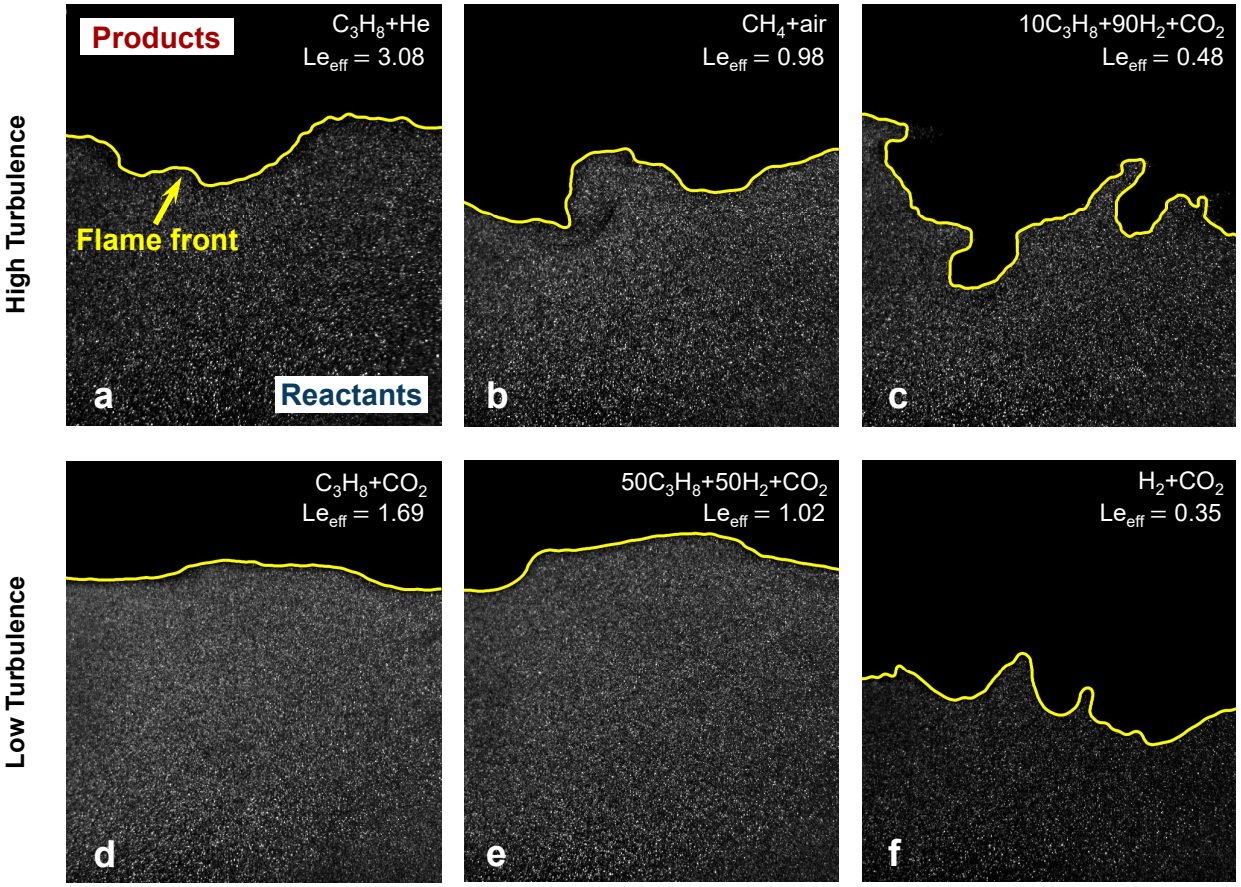

Figure 8: Sample Mie scattering images and extracted flame fronts for mixtures with distinct $\mathrm{Le_{eff}}$ at two levels of turbulence intensity. In these frames, $\overline{|\kappa|}_t \approx \langle|\kappa|\rangle$.

with $\mathrm{Le_{eff}} \lesssim 0.75$, due to the effects of differential diffusion.

3.3. Turbulent flame structure

The effects of $\mathrm{Le_{eff}}$ on turbulent flame-front curvature (κ), and creating/enhancing FSA, are illustrated in Figs. 8a−8f, where sample Mie scattering images and extracted flame fronts for mixtures with distinct $\mathrm{Le_{eff}}$ are demonstrated at two levels of turbulence intensity. The representative frames are chosen so that the average absolute curvature within the test domain of the chosen frame at time t is close to the most-probable absolute curvature over the whole image sequence, i.e., $\overline{|\kappa|}_t \approx \langle|\kappa|\rangle$. These instantaneous frames illustrate a significant increase in flame-front curvature and FSA for thermo-diffusively unstable mixtures with $\mathrm{Le_{eff}} \ll 1$ at each turbulence intensity.

The uncertainties in κ and Σ measurements originate from the uncertainties in the flame-front tracking method, which defines the resolution of the measurement technique in recognizing κ and Σ. In these experiments, the total uncertainty in tracking the flame location is less than $0.5\,\delta_\mathrm{L}$ ($\approx 0.2\,\mathrm{mm}$) [37, 38], which implies that the maximum κ that can be measured is $\approx 5000\,\mathrm{m}^{-1}$. The flame-front curvature associated with the same scale as

the average flame thickness, and the average integral length scale, are $(1/\delta_{\mathrm{L}}) \approx 2500\,\mathrm{m}^{-1}$, and $(1/L) \approx 350\,\mathrm{m}^{-1}$, respectively, which are well below the maximum resolution limit. The Kolmogorov scale significantly increases in the flame region due to high temperatures. Available measurements of flame-front wrinkles, summarized in [19], show that the characteristic length of wrinkles in the flame front is never as small as the cold-flow (inlet) Kolmogorov length scale, or even the Taylor scale. Driscoll [19] also points out that only turbulent eddies larger than 20 % of L are strong enough to wrinkle the flame, and create/increase flame-front perturbations. The initial Kolmogorov eddies at the nozzle exit are too weak and they may be easily destroyed by viscosity; hence, they are not strong enough to perturb the flame nor to create wrinkles. The discussion above shows that the measurement technique employed has a sufficient resolution to quantify the effects of differential diffusion and turbulence on both κ and Σ.

3.3.1. Flame-front curvature

In turbulent flames, eddies enhance the stretch imposed on flames through increasing flamelet curvature. The effects of differential diffusion on flame-front curvature are illustrated in Fig. 9. Curvature PDFs display a symmetric profile with a near-zero mean in all turbulent flames ($\langle\kappa\rangle \approx 0$), as illustrated in Fig. 9a. It was illustrated in previous studies that the skewness of the local flame curvature PDF is a suitable parameter for identifying the presence of Darrieus–Landau (DL) hydrodynamic instabilities [94, 95]. The large negative curvature values associated with the DL instabilities lead to a PDF profile with a distinct asymmetry, where $\langle\kappa\rangle < 0$. Therefore, Fig. 9a shows that the fluctuations are not associated with the DL instabilities, and the flame-front curvature is equally negative as it is positive for all $\mathrm{Le}_{\mathrm{eff}}$ values. Fogla *et al.* [96] also showed that with increasing turbulence intensity, DL instabilities are weakened, and the effects of turbulence become more prominent. On the other hand, Fig. 9b illustrates that, at both turbulence intensities, $\langle|\kappa|\rangle$ is almost constant in thermo-diffusively stable mixtures with $\mathrm{Le}_{\mathrm{eff}} > 1$, whereas it significantly increases with decreasing $\mathrm{Le}_{\mathrm{eff}}$ in thermo-diffusively unstable mixtures with $\mathrm{Le}_{\mathrm{eff}} < 1$, due to variations in mixtures transport properties. As illustrated in Fig. 9b, at the higher turbulence intensity, the average magnitude of the flame curvature, $\langle|\kappa|\rangle$, is larger compared to the lower intensity case, consistent with Fig. 8, as the size spectrum of the turbulent eddies are extended towards smaller scales, and that the small eddies have become stronger and the dissipation of their energy by viscous forces are delayed; hence, these eddies are more effective in increasing κ. The discussion above shows that turbulent flames in the thin reaction zone regime are controlled by both turbulence and the effects of differential diffusion in thermo-diffusively unstable mixtures ($\mathrm{Le}_{\mathrm{eff}} < 1$), whereas they are controlled solely by turbulence in thermo-diffusively stable mixtures ($\mathrm{Le}_{\mathrm{eff}} > 1$) [97].

3.3.2. Flame-surface area

Variations of the most-probable FSA of turbulent flames normalized by the FSA of a laminar flame ($\langle\Sigma\rangle \approx \langle A_{\mathrm{T}}\rangle/A_{\mathrm{L}}$) with respect to $\mathrm{Le}_{\mathrm{eff}}$ are shown in Fig. 10a. This figure shows that increasing turbulence intensity increases $\langle\Sigma\rangle$ due to the effects of more-intense eddies in creating FSA, consistent with recent studies (e.g., [96]). Figure 10a illustrates that,

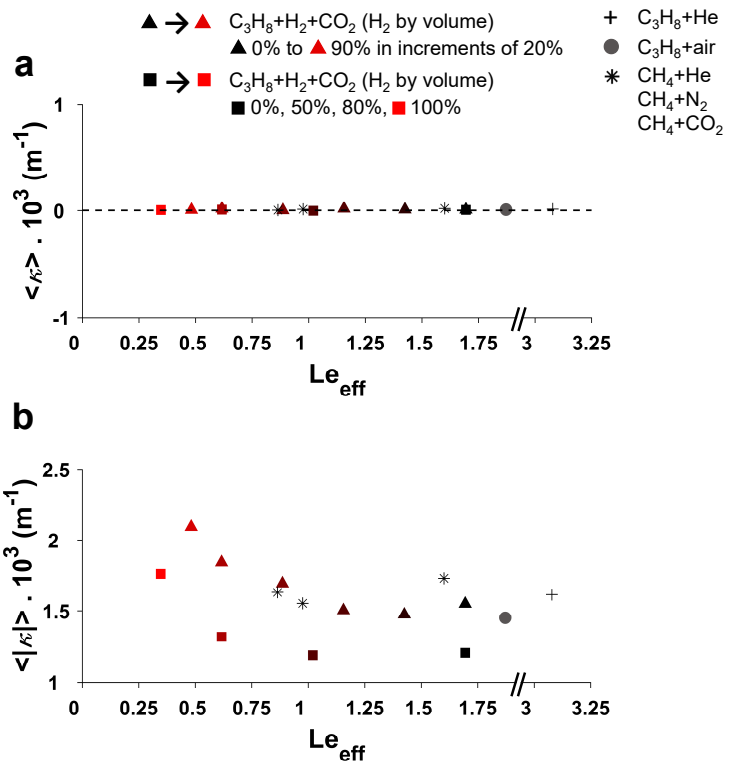

Figure 9: Flame-front curvature at various $\mathrm{Le_{eff}}$: (a) $\langle\kappa\rangle$, (b) $\langle|\kappa|\rangle$. The x-axis is broken to show the C_3H_8-He flame at $\mathrm{Le_{eff}} = 3.08$.

in mixtures with $\mathrm{Le_{eff}} > 1$, $\langle\Sigma\rangle$ is almost constant; whereas, as $\mathrm{Le_{eff}}$ falls below unity, $\langle\Sigma\rangle$ increases with decreasing $\mathrm{Le_{eff}}$ at both turbulence intensities. This figure also demonstrates that the increase in $\langle\Sigma\rangle$ by changing $\mathrm{Le_{eff}}$ is comparable to the enhancement of FSA caused by increasing turbulence intensity by approximately 50 %. Similar scaling was observed in a previous DNS study of turbulent premixed flames in the thin reaction zone regime [53]. The dependence of $\langle\Sigma\rangle$ on flame-front curvature is illustrated in Fig. 10b, where a linear correlation is shown between $\langle\Sigma\rangle$ and $\langle|\kappa|\rangle$. These results demonstrate that differential diffusion causes an increase in FSA at constant turbulence intensity.

3.4. Flame-front stretch

While laminar flames are stretched only due to the tangential hydrodynamic strain rate (K_{s-t}), turbulent flames are stretched due to both K_{s-t} and the stretch effects of turbulent eddies through increasing flamelet curvature, as illustrated in Eq. 1. The two components of flame stretch are plotted in Fig. 11. Variations of the most-probable stretch imposed on turbulent flames due to flame curvature ($\langle\kappa\, S_T\rangle$) are shown in Fig. 11a. This figure shows that the PDFs of $\kappa\, S_T$ are normally distributed around zero with slight deviations towards the positively stretched flamelets for mixtures with $\mathrm{Le_{eff}} \ll 1$, which is consistent with $\langle\kappa\rangle \approx 0$ observed in Fig. 9a, as the flame-front fluctuates around the average flame

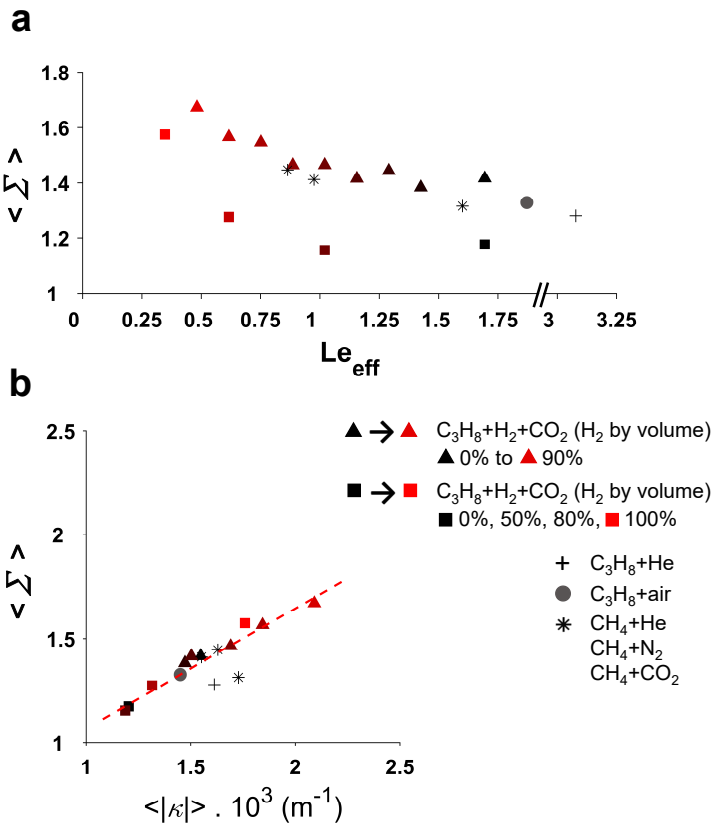

Figure 10: (a) Variations of $\langle \Sigma \rangle$ at various $\mathrm{Le_{eff}}$. The x-axis is broken to show the C_3H_8-He flame at $\mathrm{Le_{eff}} = 3.08$. (b) Correlations of $\langle \Sigma \rangle$ and $\langle |\kappa| \rangle$. Dashed line shows a linear fit: $\langle \Sigma \rangle = 0.577\ (\langle |\kappa| \rangle \times 10^3) + 0.492$.

location.

In order to highlight the effects of differential diffusion on the leading points of the flame front, the statistics of positively stretched flamelets are illustrated in Fig. 11b. Each segment of the flame front is positively stretched ($\kappa\, S_T > 0$) when: (1) it is positively curved and the leading edge velocity is positive, i.e., the flame moves towards the unburned reactants in the laboratory coordinate system, or (2) it is negatively curved and moves farther away from the fresh reactants. PDFs of S_T (Fig. 7) illustrate that $\approx 86\,\%$ of the measured S_T values are positive; hence, $\approx 86\,\%$ of the data used in PDFs of flame stretch in Fig. 9b are positively curved leading edges of the flame propagating into the fresh reactants. It is illustrated in Fig. 9b that $\langle (\kappa\, S_T)_{>0} \rangle$ increases with decreasing $\mathrm{Le_{eff}}$ in mixtures with $\mathrm{Le_{eff}} < 1$, and is larger at higher turbulence intensities, consistent with flame speed and curvature data (Figs. 7d and 9b).

The tangential hydrodynamic strain rates (K_{s-t}) for flames at various $\mathrm{Le_{eff}}$ are illustrated in Fig. 11c. In general, the two components of flame stretch in Figs. 11b and 11c show that the stretch caused by curvature is larger than the bulk strain rate in the highly turbulent flame experiments. The $\langle K_{s-t} \rangle$ remains almost constant in laminar and turbulent flames at

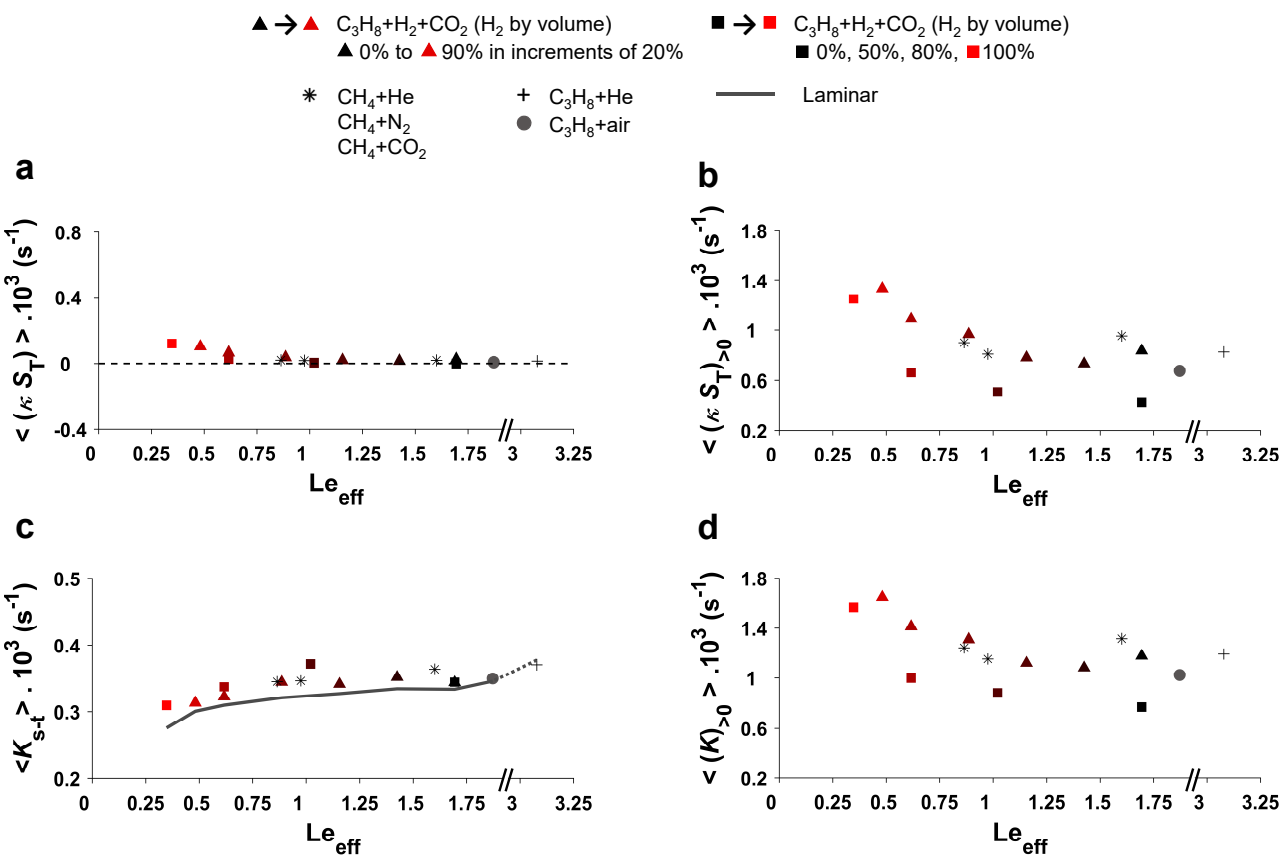

Figure 11: Components of flame stretch at various $\mathrm{Le_{eff}}$: (a) stretch imposed on turbulent flames due to flame curvature, (b) positive stretch imposed on turbulent flames due to flame curvature, (c) tangential hydrodynamic strain rate in turbulent and laminar flames, (d) total positive flame stretch imposed on turbulent flames. The x-axis is broken to show the C_3H_8-He flame at $\mathrm{Le_{eff}} = 3.08$.

various $\mathrm{Le_{eff}}$, with the average value $\approx 336\,\mathrm{s^{-1}}$, as the bulk-flow velocity is constant in all experiments.

The most-probable total stretch imposed on turbulent flames is calculated using Eq. 1, and plotted against $\mathrm{Le_{eff}}$ in Fig. 11d for positively stretched flame-front segments. These results show values in the range of $700\,\mathrm{s^{-1}} \lesssim \langle K_{>0} \rangle \lesssim 1600\,\mathrm{s^{-1}}$. Variations of $\langle K_{>0} \rangle$ show that the total stretch imposed on the leading points of the flame front increases with decreasing $\mathrm{Le_{eff}}$ for thermo-diffusively unstable mixtures with $\mathrm{Le_{eff}} < 1$.

3.5. Turbulent burning rate

The effects of differential diffusion on the burning rate of turbulent premixed flames include the effects of local flamelet displacement velocity, as well as the effects of FSA, as illustrated in Eq. 2. Equation 2 is used to calculate the instantaneous turbulent burning rate ($S_{\mathrm{T-LC}}$) for flames with various $\mathrm{Le_{eff}}$, using the Σ and the average normalized S_{T} ($I_{\mathrm{o}} \approx S_{\mathrm{T}}/S_{\mathrm{L}}^{\mathrm{o}}$), over the entire flame front within the test domain, at time t. In order to quantify the effects of I_{o} and Σ on $S_{\mathrm{T-LC}}$, the most-probable turbulent burning rate $\langle S_{\mathrm{T-LC}} \rangle$

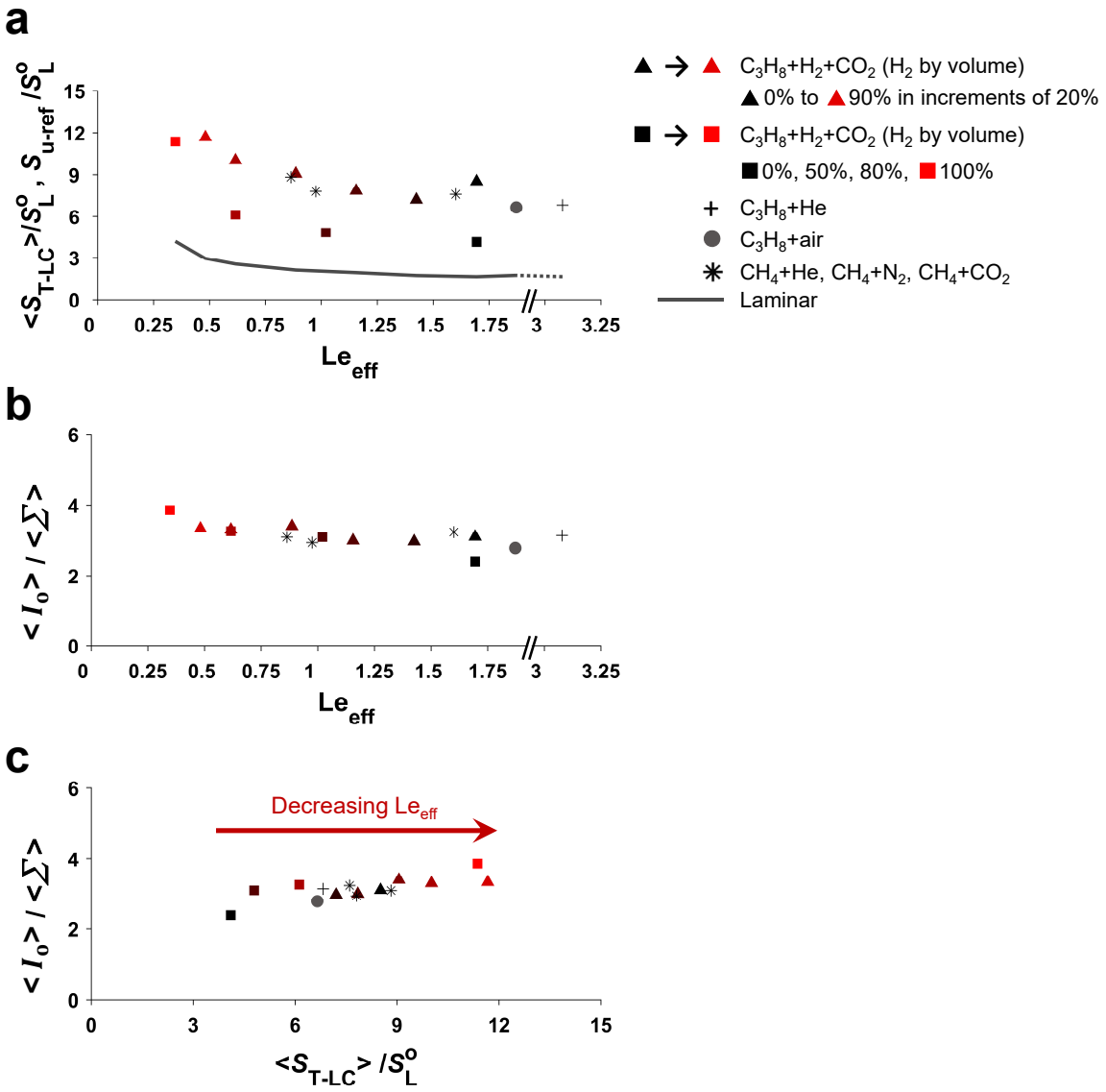

Figure 12: (a) Turbulent burning rates at various $\mathrm{Le_{eff}}$ in turbulent flames compared to reference flame speeds in laminar flames. The x-axis is broken to show the C_3H_8-He flame at $\mathrm{Le_{eff}} = 3.08$. The relative contribution of the normalized $\langle S_T \rangle$ ($\langle I_o \rangle = \langle S_T \rangle / S_L^o$) and $\langle \Sigma \rangle$ in increasing S_{T-LC} are plotted against: (b) $\mathrm{Le_{eff}}$, and (c) normalized $\langle S_{T-LC} \rangle$.

is extracted from the time series of S_{T-LC}, and plotted in Fig. 12a for various $\mathrm{Le_{eff}}$. S_{u-ref}/S_L^o values are also included to show the burning rate of laminar flames. The S_{T-LC} is almost constant with decreasing $\mathrm{Le_{eff}}$ in mixtures with $\mathrm{Le_{eff}} > 1$, and increases when $\mathrm{Le_{eff}}$ falls below unity. The effect of $\mathrm{Le_{eff}}$ on the burning rates of premixed stretched flames is not linear, with sharp increases in flames with $\mathrm{Le_{eff}} \lesssim 0.75$ in both laminar and turbulent flames. The differences in the S_{T-LC} of laminar and turbulent flames are due to the effects of turbulent

eddies in increasing flame stretch and creating/enhancing FSA, which results in increasing flame burning rates.

The ratio of the effects of the most-probable I_o and the most-probable Σ in increasing S_{T-LC} is plotted against Le_{eff} and the normalized S_{T-LC} in Figs. 12b and 12c, respectively. As shown in these figures, the ratio of these two parameters is almost constant ($\langle I_o \rangle / \langle \Sigma \rangle \approx 3.1$), and the results overlap over the wide range of Lewis numbers, and turbulence intensities, used in these experiments. The relative contribution of these two parameters in increasing S_{T-LC} can be obtained from this ratio. This analysis shows that I_o is responsible for approximately 76 % of the observed S_{T-LC}, and the remaining 24 % results from increasing FSA. This result shows the essential role of differential diffusion on turbulent burning rates, which needs to be considered in the study of turbulent flames.

3.6. Discussion – The effects of differential diffusion on turbulent burning rates

Variations of turbulent burning rates with decreasing Le_{eff}, illustrated in Fig. 12a, correlate closely with flame location (Figs. 5b and 5d), local flamelet displacement velocity (Fig. 7d), flame-front curvature (Fig. 9b), flame-surface area (Fig. 10a), and flame stretch (Fig. 11d) at various Le_{eff}. These results are consistent with the idea that, in thermo-diffusively unstable mixtures with $Le_{eff} < 1$, when the flame front is perturbed, thermal-diffusive (TD) instabilities cause two main effects on flame propagation: (1) at the positively stretched portion of the flame front, the local velocity increases towards the fresh reactants due to the effects of differential diffusion, and (2) as the reactants approach the reaction zone in the negatively curved region along two side-by-side positively curved segments of the flame front, the fuel will preferentially diffuse out of the fresh reactants towards the positively curved leading edges, due to the higher molecular diffusion of the lighter fuels compared to the heavier oxidizer (i.e., preferential diffusion), and make the reactants leaner as they approach the reaction zone. This will decrease the propagation velocity in the negatively curved region; hence, the positively and negatively curved segments of the flame front move farther away from the average flame location. As illustrated in Fig. 9a, PDFs of curvature display a symmetric profile with a near-zero mean even for thermo-diffusively unstable mixtures with $Le_{eff} < 1$, with no skewness towards positive curvature values. This shows that the flame-front curvature is equally negative as it is positive, and that the increase in the average magnitude of flame curvature shown in Fig. 9b is primarily associated with the preferential diffusion of the lighter fuels compared to the heavier oxidizer. Similar methodology was used in [94] for identifying the presence of DL hydrodynamic instabilities based on the skewness of the flame curvature PDF. This preferential diffusion results in increasing local curvature and stretch imposed on that location along the flame front, which further triggers the effects of differential diffusion in increasing local velocity, curvature, and flame stretch. Both these effects further amplify the initial wrinkle, and lead to a flame that has a larger FSA, which burns more reactants, and has higher local flamelet velocities; both effects increasing the flame burning rates. Increasing average flame burning rates causes the thermo-diffusively unstable flames to climb up the steep bulk velocity gradients in the stagnation flow, resulting in a significant relocation of these flames towards the bottom nozzle (Figs. 5b and 5d), and eventually leading to flash back in mixtures with $Le_{eff} \ll 1$. Flash

back is a direct result of these higher turbulent burning rates due to variations in diffusive properties, at constant laminar flame speed, bulk flow velocity, and turbulence intensity.

There are two main mechanisms that limit the perpetual increase in local flame velocities and burning rates: (1) the destruction of FSA due to the flame-front segments merging at the trailing points, forming cusps, which reduces the flame-front curvature and flame stretch, leading to flamelets with smaller FSA, lower local velocities, and smaller flame burning rates, and (2) the propagation of leading points in all directions, which means that their radius of curvature increases in time, leading to a lower curvature; hence, putting a limit on the maximum flamelet velocity in that location along the flame front. Therefore, the average burning rate causes the flames to stabilize at some average location within the steep bulk-velocity gradients of the counterflow.

As illustrated in Fig. 7d and Fig. 12a, the same overall curve of S_{T} versus $\mathrm{Le}_{\mathrm{eff}}$, as well as for $S_{\mathrm{T-LC}}$ versus $\mathrm{Le}_{\mathrm{eff}}$, are obtained for all mixtures, regardless of the fuel composition or inert gases used. These results indicate that the values of S_{T} and $S_{\mathrm{T-LC}}$, measured over a wide range of Lewis numbers, are not dependent on the fuel or oxidizing-gas mixture, and can be described fully by $\mathrm{Le}_{\mathrm{eff}}$ and turbulence intensity. Furthermore, Figs. 12b and 12c illustrate that the relative contribution of local flamelet velocities and FSA in increasing $S_{\mathrm{T-LC}}$ is not dependent on the fuel, oxidizing-gas mixture, or turbulence intensity, and the results overlap over a wide range of Lewis numbers.

Figure 10a show that increasing turbulence intensity increases the FSA. In addition, Figs. 9b and 11d illustrate that increasing turbulence intensity increases the effects of differential diffusion in thermo-diffusively unstable mixtures ($\mathrm{Le}_{\mathrm{eff}} < 1$). At higher turbulence intensities, the size spectrum of the turbulent eddies are extended towards smaller scales, the small eddies contain more turbulence kinetic energy, and the dissipation of their energy by viscous forces are delayed; hence, these eddies are more effective in increasing the stretch imposed on flames through increasing flamelet curvature. These effects demonstrate that the effects of turbulence and differential diffusion are linked in increasing turbulent burning rates in mixtures with $\mathrm{Le}_{\mathrm{eff}} < 1$.

Flame-front cellular instabilities in premixed flames arise from a combination of both TD and DL hydrodynamic instabilities. While DL instabilities are typically neglected for small-scale flames at atmospheric pressure, due to the diffusional thickness of the flame, these effects are coupled to the effects of differential diffusion at high-pressure combustion for which DL instabilities can be substantially enhanced due to very thin flames. Recent studies show that turbulence triggers the production of instabilities, and may act to accentuate the burning rate by promoting intrinsic flame instabilities [52, 98], consistent with the observations of this study that for thermo-diffusively unstable flames, turbulence increases both S_{T} and Σ. The discussion above shows that the effects of turbulence intensity, TD instabilities, and DL hydrodynamic instabilities may be interlinked during turbulent premixed flame propagation of mixtures with $\mathrm{Le}_{\mathrm{eff}} < 1$. Furthermore, in turbulent premixed flames, the local flame conformation, and overall combustion properties, such as turbulent burning rates and flame structure, are influenced by advection of these instabilities along the flame surface referred to as a *memory effect* [19]. This phenomenon suggests that the burning rate and morphology of turbulent flames depend on both mixture properties, as well

as geometry-dependent parameters [19, 94], which can be accounted for by the mean flame stretch modulated by the Markstein length [94], the former implicitly accounts for geometry-dependence [19], and the latter accounts for all diffusion processes occurring inside the flame zone [94]. The results represented in this study are consistent with this understanding.

While turbulence and DL hydrodynamic instabilities interact in the wrinkled/corrugated flamelet regimes, it was shown that for high turbulence intensities the effects of DL instabilities are predicted to diminish, and the flames are dominated by the turbulence in the vicinity of the thin reaction zone regime, in the corrugated flamelet regime [96, 97]. However, the results of this study show that TD instabilities are effective in increasing turbulent flame speed even for highly turbulent flames, and there is currently no theory to predict these physics. This work therefore shows the need to advance combustion theory to produce models that can capture these effects for flames in real-world combustion systems to predict the performance of future fuel-flexible combustors, and the present results provide a valuable dataset for the validation of such theories.

4. Conclusions

The effects of differential diffusion on lean turbulent premixed flame location, local flamelet velocities, burning rates, and flame structure were investigated using counter-flow flames in the thin reaction zone regime. Various fuel-oxidizer-inert mixtures representative of a wide range of Lewis numbers were used in the context of fuel flexibility. Local instantaneous statistics of various flame parameters within the imaged plane were quantified as probability density functions using sufficiently large data sets to ensure statistical accuracy. These statistics showed that the effects of differential diffusion on the burning rates and the structure of turbulent premixed flames are important in the thin reaction zone regime ($1 < \mathrm{Ka_T} < 100$ and $\mathrm{Da_T} < 1$), and turbulence does not mask these effects, even if turbulent heat and mass transport are significantly enhanced over the laminar values.

The PDFs showed that, in turbulent premixed flames, local flamelet velocities and turbulent burning rates increase with decreasing $\mathrm{Le_{eff}}$ at constant turbulence intensity and laminar flame speed. In addition to increasing local flamelet velocities, differential diffusion also increases both flame-front curvature and flame-surface area in mixtures with $\mathrm{Le_{eff}} < 1$ at constant turbulence intensity, which increases turbulent burning rates. The effects of Lewis number are not linear; most results remain almost constant in mixtures with $\mathrm{Le_{eff}} > 1$, whereas they increase sharply with decreasing $\mathrm{Le_{eff}}$ in mixtures with $\mathrm{Le_{eff}} \lesssim 0.75$. The relative contribution of turbulent flamelet velocities and flame-surface area, in increasing turbulent burning rates, is approximately 76 % and 24 %, respectively, and this proportion is not dependent on the fuel, oxidizing-gas mixture, or turbulence intensity, and the results overlap over a wide range of Lewis numbers. Furthermore, local flamelet velocities, burning rates, and structure parameters, i.e., flame-front curvature and flame-surface area, increase with increasing turbulence intensity, as commonly understood.

These results show that the effects of differential diffusion on turbulent premixed flame propagation of thermo-diffusively unstable mixtures in the thin reaction zone regime include the explicit effects on both increasing local flamelet displacement velocity, as well as

increasing flame-surface area, as these two parameters are highly correlated. Furthermore, the effects of differential diffusion on various parameters of turbulent premixed flames, measured over a wide range of Lewis numbers, are not dependent on the fuel or oxidizing-gas mixture, and can be described fully by Le_{eff} and turbulence intensity.

Acknowledgment

This research was funded by the Natural Sciences and Engineering Research Council of Canada (grant No. I242349C0G) and Siemens Canada Limited under the Collaborative Research and Development program (NSERC-CRD). Support of the McGill Engineering Doctoral Awards (MEDA) program is also gratefully acknowledged.

Appendix. Supplementary material

Supplementary material associated with this article can be found in the online version.

References

[1] M. Z. Jacobson, M. A. Delucchi, Providing all global energy with wind, water, and solar power, part I: Technologies, energy resources, quantities and areas of infrastructure, and materials, Energy policy 39 (2011) 1154–1169.

[2] H. Ibrahim, A. Ilinca, J. Perron, Energy storage systems-characteristics and comparisons, Renew. Sust. Energ. Rev. 12 (2008) 1221–1250.

[3] L. Brennan, P. Owende, Biofuels from microalgae - A review of technologies for production, processing, and extractions of biofuels and co-products, Renew. Sust. Energ. Rev. 14 (2010) 557–577.

[4] Y. Hou, R. Vidu, P. Stroeve, Solar energy storage methods, Ind. Eng. Chem. Res. 50 (2011) 8954–8964.

[5] J. M. Bergthorson, M. J. Thomson, A review of the combustion and emissions properties of advanced transportation biofuels and their impact on existing and future engines, Renew. Sust. Energ. Rev. 42 (2015) 1393–1417.

[6] Z. Huang, Y. Zhang, K. Zeng, B. Liu, Q. Wang, D. Jiang, Measurements of laminar burning velocities for natural gas–hydrogen–air mixtures, Combust. Flame 146 (2006) 302–311.

[7] E. Hu, Z. Huang, J. He, C. Jin, J. Zheng, Experimental and numerical study on laminar burning characteristics of premixed methane–hydrogen–air flames, Int. J. Hydrogen Energy 34 (2009) 4876–4888.

[8] C. Tang, Z. Huang, C. Jin, J. He, J. Wang, X. Wang, H. Miao, Laminar burning velocities and combustion characteristics of propane–hydrogen–air premixed flames, Int. J. Hydrogen Energy 33 (2008) 4906–4914.

[9] P. Strakey, T. Sidwell, J. Ontko, Investigation of the effects of hydrogen addition on lean extinction in a swirl stabilized combustor, Proc. Combust. Inst. 31 (2007) 3173–3180.

[10] F. Halter, C. Chauveau, I. Gökalp, Characterization of the effects of hydrogen addition in premixed methane/air flames, Int. J. Hydrogen Energy 32 (2007) 2585–2592.

[11] B. Karlovitz, D. Denniston Jr, D. Knapschaefer, F. Wells, Studies on turbulent flames: A. Flame propagation across velocity gradients B. Turbulence measurement in flames, Symp. (Int.) Combust. 4 (1953) 613–620.

[12] M. Matalon, On flame stretch, Combust. Sci. Technol. 31 (1983) 169–181.

[13] A. Buschmann, F. Dinkelacker, T. Schäfer, M. Schäfer, J. Wolfrum, Measurement of the instantaneous detailed flame structure in turbulent premixed combustion, Symp. (Int.) Combust. 26 (1996) 437–445.

[14] Ö. L. Gülder, G. J. Smallwood, Flame surface densities in premixed combustion at medium to high turbulence intensities, Combust. Sci. Technol. 179 (2007) 191–206.

[15] F. T. Yuen, Ö. L. Gülder, Turbulent premixed flame front dynamics and implications for limits of flamelet hypothesis, Proc. Combust. Inst. 34 (2013) 1393–1400.
[16] R. W. Pitz, S. Hu, P. Wang, Tubular premixed and diffusion flames: Effect of stretch and curvature, Prog. Energy Combust. Sci. 42 (2014) 1–34.
[17] L. P. H. De Goey, T. Plessing, R. Hermanns, N. Peters, Analysis of the flame thickness of turbulent flamelets in the thin reaction zones regime, Proc. Combust. Inst. 30 (2005) 859–866.
[18] R. Sankaran, E. R. Hawkes, J. H. Chen, T. Lu, C. K. Law, Structure of a spatially developing turbulent lean methane–air bunsen flame, Proc. Combust. Inst.e 31 (2007) 1291–1298.
[19] J. F. Driscoll, Turbulent premixed combustion: Flamelet structure and its effect on turbulent burning velocities, Prog. Energy Combust. Sci. 34 (2008) 91–134.
[20] F. T. Yuen, Ö. L. Gülder, Dynamics of lean-premixed turbulent combustion at high turbulence intensities, Combust. Sci. Technol. 182 (2010) 544–558.
[21] A. Marshall, J. Lundrigan, P. Venkateswaran, J. Seitzman, T. Lieuwen, Fuel effects on leading point curvature statistics of high hydrogen content fuels, Proc. Combust. Inst. 35 (2015) 1417–1424.
[22] G. Damköhler, The effect of turbulence on the combustion rate in gas compounds, Z. Elektrochem. Angew. Phys. Chem. 46 (1940) 601–626.
[23] C. K. Law, Dynamics of stretched flames, Symp. (Int.) Combust. 22 (1989) 1381–1402.
[24] J. Tien, M. Matalon, On the burning velocity of stretched flames, Combust. Flame 84 (1991) 238–248.
[25] F. A. Williams, Progress in knowledge of flamelet structure and extinction, Prog. Energy Combust. Sci. 26 (2000) 657–682.
[26] A. Lipatnikov, J. Chomiak, Molecular transport effects on turbulent flame propagation and structure, Prog. Energy Combust. Sci. 31 (2005) 1–73.
[27] C. K. Law, Combustion physics, Cambridge University Press, Cambridge, UK, 2010.
[28] P. A. Libby, F. A. Williams, Structure of laminar flamelets in premixed turbulent flames, Combust. Flame 44 (1982) 287–303.
[29] Y.-C. Chen, R. W. Bilger, Experimental investigation of three-dimensional flame-front structure in premixed turbulent combustion: II. Lean hydrogen/air bunsen flames, Combust. Flame 138 (2004) 155–174.
[30] A. Amato, M. Day, R. Cheng, J. Bell, T. Lieuwen, Leading edge statistics of turbulent, lean, H_2–air flames, Proc. Combust. Inst. 35 (2015) 1313–1320.
[31] P. Venkateswaran, A. Marshall, D. H. Shin, D. Noble, J. Seitzman, T. Lieuwen, Measurements and analysis of turbulent consumption speeds of H_2/CO mixtures, Combust. Flame 158 (2011) 1602–1614.
[32] H. Kobayashi, T. Tamura, K. Maruta, T. Niioka, F. A. Williams, Burning velocity of turbulent premixed flames in a high-pressure environment, Symp. (Int.) Combust. 26 (1996) 389–396.
[33] K. Yamamoto, M. Ozeki, N. Hayashi, H. Yamashita, Burning velocity and OH concentration in premixed combustion, Proc. Combust. Inst. 32 (2009) 1227–1235.
[34] J. Furukawa, T. Hirano, F. A. Williams, Burning velocities of flamelets in a turbulent premixed flame, Combust. Flame 113 (1998) 487–491.
[35] J. Furukawa, F. A. Williams, Flamelet effects on local flow in turbulent premixed Bunsen flames, Combust. Sci. Technol. 175 (2003) 1835–1858.
[36] Y. Ikeda, J. Kojima, T. Nakajima, F. Akamatsu, M. Katsuki, Measurement of the local flamefront structure of turbulent premixed flames by local chemiluminescence, Proc. Combust. Inst. 28 (2000) 343–350.
[37] E. Abbasi-Atibeh, J. M. Bergthorson, Differential diffusion effects in counter-flow premixed hydrogen-enriched methane and propane flames, Proc. Combust. Inst. 37 (2019) 2399–2406.
[38] E. Abbasi-Atibeh, S. Jella, J. M. Bergthorson, Fuel variation effects in propagation and stabilization of turbulent counter-flow premixed flames, J. Eng. Gas Turb. Power 141 (2018) 031024.
[39] K. N. C. Bray, R. Cant, Some applications of Kolmogorov's turbulence research in the field of combustion, Proc. R. Soc. London, Ser. A 434 (1991) 217–240.
[40] S. Kheirkhah, Ö. L. Gülder, Consumption speed and burning velocity in counter-gradient and gradient diffusion regimes of turbulent premixed combustion, Combust. Flame 162 (2015) 1422–1439.

[41] J. D. Regele, E. Knudsen, H. Pitsch, G. Blanquart, A two-equation model for non-unity Lewis number differential diffusion in lean premixed laminar flames, Combust. Flame 160 (2013) 240–250.
[42] S. D. Salusbury, J. M. Bergthorson, Maximum stretched flame speeds of laminar premixed counter-flow flames at variable Lewis number, Combust. Flame 162 (2015) 3324–3332.
[43] R. Abdel-Gayed, D. Bradley, M. Hamid, M. Lawes, Lewis number effects on turbulent burning velocity, Symp. (Int.) Combust. 20 (1984) 505–512.
[44] D. Bradley, How fast can we burn?, Symp. (Int.) Combust. 24 (1992) 247–262.
[45] R. S. Barlow, M. J. Dunn, M. S. Sweeney, S. Hochgreb, Effects of preferential transport in turbulent bluff-body-stabilized lean premixed CH_4/air flames, Combust. Flame 159 (2012) 2563–2575.
[46] E. Boschek, P. Griebel, P. Jansohn, Fuel variability effects on turbulent, lean premixed flames at high pressures, Proceedings of the ASME Turbo Expo: Turbine Technical Conference and Exposition (2007) GT2007–27496.
[47] F. Dinkelacker, B. Manickam, S. Muppala, Modelling and simulation of lean premixed turbulent methane/hydrogen/air flames with an effective Lewis number approach, Combust. Flame 158 (2011) 1742–1749.
[48] V. Kuznetsov, V. Sabel'nikov, P. Libby, Turbulence and Combustion, Hemisphere Publishing, Moscow, Russia, 1986.
[49] V. Karpov, A. Lipatnikov, V. Zimont, Flame curvature as a determinant of preferential diffusion effects in premixed turbulent combustion, Progress in Astronautics and Aeronautics, Adv. Combust. Sci.: In Honor of Ya. B. Zel'dovich 173 (1997) 235–250.
[50] S. Yang, A. Saha, W. Liang, F. Wu, C. K. Law, Extreme role of preferential diffusion in turbulent flame propagation, Combust. Flame 188 (2018) 498–504.
[51] B. Savard, G. Blanquart, Broken reaction zone and differential diffusion effects in high Karlovitz n-C_7H_{16} premixed turbulent flames, Combust. Flame 162 (2015) 2020–2033.
[52] Z. Liu, S. Yang, C. K. Law, A. Saha, Cellular instability in Le$<$ 1 turbulent expanding flames, Proc. Combust. Inst. 37 (2019) 2611–2618.
[53] I. Han, K. Y. Huh, Roles of displacement speed on evolution of flame surface density for different turbulent intensities and Lewis numbers in turbulent premixed combustion, Combust. Flame 152 (2008) 194–205.
[54] P. J. Goix, I. Shepherd, Lewis number effects on turbulent premixed flame structure, Combust. Sci. Technol. 91 (1993) 191–206.
[55] R. Borghi, On the structure and morphology of turbulent premixed flames, Recent Adv. Aerosp. Sci. (1985) 117–138.
[56] N. Peters, Turbulent combustion, Cambridge University Press, Cambridge, UK, 2000.
[57] L. Kostiuk, K. Bray, T. Chew, Premixed turbulent combustion in conterflowing streams, Combust. Sci. Technol. 64 (1989) 233–241.
[58] E. Mastorakos, A. Taylor, J. Whitelaw, Extinction and temperature characteristics of turbulent counterflow diffusion flames with partial premixing, Combust. Flame 91 (1992) 40–54.
[59] L. Kostiuk, K. Bray, R. Cheng, Experimental study of premixed turbulent combustion in opposed streams: Part I—Nonreacting flow field, Combust. Flame 92 (1993) 377–395.
[60] L. Kostiuk, K. Bray, R. Cheng, Experimental study of premixed turbulent combustion in opposed streams: Part II–Reacting flow field and extinction, Combust. Flame 92 (1993) 396–409.
[61] E. Mastorakos, A. Taylor, J. Whitelaw, Extinction of turbulent counterflow flames with reactants diluted by hot products, Combust. Flame 102 (1995) 101–114.
[62] K. Sardi, A. Taylor, J. Whitelaw, Conditional scalar dissipation statistics in a turbulent counterflow, J. Fluid Mech. 361 (1998) 1–24.
[63] L. Kostiuk, I. Shepherd, K. Bray, Experimental study of premixed turbulent combustion in opposed streams. Part III–Spatial structure of flames, Combust. Flame 118 (1999) 129–139.
[64] D. Geyer, A. Kempf, A. Dreizler, J. Janicka, Turbulent opposed-jet flames: A critical benchmark experiment for combustion LES, Combust. Flame 143 (2005) 524–548.
[65] G. Coppola, B. Coriton, A. Gomez, Highly turbulent counterflow flames: A laboratory scale benchmark

for practical systems, Combust. Flame 156 (2009) 1834–1843.
[66] F. Hampp, R. Lindstedt, Quantification of combustion regime transitions in premixed turbulent DME flames, Combust. Flame 182 (2017) 248–268.
[67] A. Kempf, H. Forkel, J.-Y. Chen, A. Sadiki, J. Janicka, Large-eddy simulation of a counterflow configuration with and without combustion, Proc. Combust. Inst. 28 (2000) 35–40.
[68] D. G. Goodwin, H. K. Moffat, R. L. Speth, Cantera: A software toolkit for chemical kinetics, thermodynamics, and transport processes, Version 2.2.1, http://www.cantera.org (2016).
[69] N. Bouvet, F. Halter, C. Chauveau, Y. Yoon, On the effective Lewis number formulations for lean hydrogen/hydrocarbon/air mixtures, Int. J. Hydrogen Energy 38 (2013) 5949–5960.
[70] H. W. Liepmann, Investigations on laminar boundary-layer stability and transition on curved boundaries, NACA Wartime Report W-107. ACR No. 3H30, Technical Report, 1943.
[71] J. M. Bergthorson, Experiments and modeling of impinging jets and premixed hydrocarbon stagnation flames, PhD thesis, California Institute of Technology, 2005.
[72] G. Coppola, A. Gomez, Experimental investigation on a turbulence generation system with high-blockage plates, Exp. Therm Fluid Sci. 33 (2009) 1037–1048.
[73] B. Böhm, O. Stein, A. Kempf, A. Dreizler, In-nozzle measurements of a turbulent opposed jet using PIV, Flow Turbul. Combust. 85 (2010) 73–93.
[74] G. E. Glawe, R. Holanda, L. N. Krause, Recovery and radiation corrections and time constants of several sizes of shielded and unshielded thermocouple probes for measuring gas temperature, NASA: NASA-TP-1099, E-9289, Technical Report, 1978.
[75] V. Hindasageri, R. P. Vedula, S. V. Prabhu, Thermocouple error correction for measuring the flame temperature with determination of emissivity and heat transfer coefficient, Rev. Sci. Instrum. 84 (2013) 024902.
[76] S. Kruse, P. R. Medwell, J. Beeckmann, H. Pitsch, The significance of beam steering on laser-induced incandescence measurements in laminar counterflow flames, Appl. Phys. B 124 (2018) 212–222.
[77] H. Tennekes, J. Lumley, A First Course in Turbulence, The MIT Press, Cambridge, USA, 1972.
[78] S. Pope, Turbulent flows, Cambridge University Press, Cambridge, UK, 2000.
[79] J. Hinze, Turbulence, McGraw-Hill, New York, USA, 1975.
[80] T. Lachaux, F. Halter, C. Chauveau, I. Gökalp, I. Shepherd, Flame front analysis of high-pressure turbulent lean premixed methane–air flames, Proc. Combust. Inst. 30 (2005) 819–826.
[81] S. A. Filatyev, J. F. Driscoll, C. D. Carter, J. M. Donbar, Measured properties of turbulent premixed flames for model assessment, including burning velocities, stretch rates, and surface densities, Combust. Flame 141 (2005) 1–21.
[82] T. Pavlidis, Algorithms for graphics and image processing, Springer Science & Business Media, Computer Science Press, Rockville, MD, USA, 2012.
[83] I. Shepherd, Flame surface density and burning rate in premixed turbulent flames, Symp. (Int.) Combust. 26 (1996) 373–379.
[84] J. B. Bell, M. S. Day, I. G. Shepherd, M. R. Johnson, R. K. Cheng, J. F. Grcar, V. E. Beckner, M. J. Lijewski, Numerical simulation of a laboratory-scale turbulent V-flame, Proceedings of the National Academy of Sciences 102 (2005) 10006–10011.
[85] M. Haq, C. Sheppard, R. Woolley, D. Greenhalgh, R. Lockett, Wrinkling and curvature of laminar and turbulent premixed flames, Combust. Flame 131 (2002) 1–15.
[86] Y.-C. Chen, Measurements of flame-front curvature based on Fourier transformation, Combust. Theory Model. 11 (2007) 333–349.
[87] H. Kolla, J. Rogerson, N. Swaminathan, Validation of a turbulent flame speed model across combustion regimes, Combust. Sci. Technol. 182 (2010) 284–308.
[88] P. J. Trunk, I. Boxx, C. Heeger, W. Meier, B. Böhm, A. Dreizler, Premixed flame propagation in turbulent flow by means of stereoscopic PIV and dual-plane OH-PLIF at sustained kHz repetition rates, Proc. Combust. Inst. 34 (2013) 3565–3572.
[89] G. Hartung, J. Hult, R. Balachandran, M. Mackley, C. F. Kaminski, Flame front tracking in turbulent lean premixed flames using stereo PIV and time-sequenced planar LIF of OH, Appl. Phys. B 96 (2009)

843–862.

[90] R. Abu-Gharbieh, G. Hamarneh, T. Gustavsson, C. F. Kaminski, Flame front tracking by laser induced fluorescence spectroscopy and advanced image analysis, Opt. Express 8 (2001) 278–287.

[91] R. Abu-Gharbieh, G. Hamarneh, T. Gustavsson, C. F. Kaminski, Level set curve matching and particle image velocimetry for resolving chemistry and turbulence interactions in propagating flames, J. Math. Imaging Vis. 19 (2003) 199–218.

[92] I. R. Gran, T. Echekki, J. H. Chen, Negative flame speed in an unsteady 2-D premixed flame: A computational study, Symp. (Int.) Combust. 26 (1996) 323–329.

[93] S. Daniele, J. Mantzaras, P. Jansohn, A. Denisov, K. Boulouchos, Flame front/turbulence interaction for syngas fuels in the thin reaction zones regime: turbulent and stretched laminar flame speeds at elevated pressures and temperatures, J. Fluid Mech. 724 (2013) 36–68.

[94] M. Zhang, A. Patyal, Z. Huang, M. Matalon, Morphology of wrinkles along the surface of turbulent bunsen flames–their amplification and advection due to the Darrieus–Landau instability, Proc. Combust. Inst. 37 (2019) 2335–2343.

[95] G. Troiani, F. Creta, M. Matalon, Experimental investigation of darrieus–landau instability effects on turbulent premixed flames, Proc. Combust. Inst. 35 (2015) 1451–1459.

[96] N. Fogla, F. Creta, M. Matalon, The turbulent flame speed for low-to-moderate turbulence intensities: Hydrodynamic theory vs. experiments, Combust. Flame 175 (2017) 155–169.

[97] S. Yang, A. Saha, Z. Liu, C. K. Law, Role of Darrieus–Landau instability in propagation of expanding turbulent flames, J. Fluid Mech. 850 (2018) 784–802.

[98] C. R. Bauwens, J. M. Bergthorson, S. B. Dorofeev, On the interaction of the Darrieus–Landau instability with weak initial turbulence, Proc. Combust. Inst. 36 (2017) 2815–2822.